Article:
Invernizzi, D., Pizzutto, M., Felletti, F. et al. (3 more authors) (2025) Reconstruction of the sedimentary heterogeneity in outcropping deep-water channel–levee deposits (Taza–Guercif Basin, late Tortonian, NE Morocco). Journal of Sedimentary Research, 95 (2). pp. 314-341. ISSN 1527-1404

https://doi.org/10.2110/jsr.2024.040

Reconstruction of the sedimentary heterogeneity in outcropping deep-water channel-levee deposits (Taza-Guercif Basin, late Tortonian, NE Morocco)

Invernizzi, D.[1*], Pizzutto, M.[1], Felletti, F.[1], Pantopoulos, G.[1], Marini, M.[1], McArthur, A.[2]

[1] Dipartimento di Scienze della Terra "A. Desio", Università degli Studi di Milano, Milan, Italy; [2] School of Earth and Environment, University of Leeds, Leeds, LS2 9JT, United Kingdom

**Corresponding author: daniele.invernizzi@unimi.it*

Keywords: *submarine channel, Rifian Corridor, facies architecture, outcrop, lateral accretion packages, statistics, Miocene, Tachrift*

ABSTRACT

In the context of subsurface modelling of deep-water sedimentary systems, it is crucial to confidently identify turbidite channel-levee architectural elements in ancient strata. This becomes particularly critical when working with data of limited resolution, such as wireline well or seismic data. Similarly, in areas with limited outcrop exposure, establishing the temporal relationships of channel-levee systems relies predominantly on inference. Moreover, the paucity of well-documented outcrops exhibiting continuous sedimentary record between channel-fill and overbank sediments remains a challenge.

This work presents the sedimentary architecture of channel-levee Complex 7, one of the late Tortonian (Miocene) slope channel-levee complexes constituting the Tachrift System, which records the infill of the Taza-Guercif Basin in NE Morocco. The basin was on the southern margin of an ancient seaway (the Rifian Corridor) connecting the paleo-Mediterranean Sea and the Atlantic Ocean. The objective of this study is to comprehensively document the geometry, as well as the vertical and lateral heterogeneity of facies

assemblages in the northwestern part of Complex 7. This approach encompasses geological mapping, detailed facies analysis from thirty-five sedimentary logs, and the implementation of physical stratigraphic correlations.

Facies associations and stratigraphic architecture of Complex 7 reveal an eastward channel migration and a subsequent increase in flow energy.

Due to exceptional 3D exposures, this study offers a detailed sedimentological characterization of channel fills and their correlative levee deposits. It also provides valuable insights into the evolution of the parent channel, from its formation to its abandonment, while facilitating sub-seismic-scale lithological calibration for subsurface analogs.

INTRODUCTION

Over the past decades, there has been notable progress in the sedimentological comprehension of deep-water channel systems (McHargue et al., 2011; Talling et al., 2012; Janocko et al., 2013; Talling et al., 2015; Fonnesu and Felletti, 2019; Vendettuoli et al., 2019; Hubbard et al., 2020; Tek et al., 2020; Reguzzi et al., 2023). Particular interest concerns the definition and composition of architectural elements of turbidite channel-levees (Kane et al., 2007, Morris, 2014, de Leeuw et al., 2018, Cunningham and Arnott, 2021, La Marca et al., 2023; Lewis et al., 2023; Pizzi et al., 2023; McArthur et al., 2024), sedimentary deposits found on both continental slopes and basin plains (Janocko et al., 2013). These often relatively coarse-grained architectural elements, characterized by their favorable porosity and permeability properties, are appealing targets for diverse applications such as CO_2 sequestration, underground gas storage, and groundwater exploitation (Weimer et al., 2000; Pettingill and Weimer, 2002; Abreu et al., 2003; Weimer and Pettingill, 2007; Marshall et al., 2016). As such, the sedimentary heterogeneity of channel-levees is important, as it plays a central role in the assessment of reservoir volumes and the optimization of production (Kominz et al., 2011; Kane and Clare, 2019; Pohl et al., 2020; Bell et al., 2021; Valle-Falcones et al., 2023).

Despite advances in seismic data acquisition, which yield detailed 3D subsurface images (Wynn et al., 2007; Janocko et al., 2013; Jobe et al., 2015; Hubbard et al., 2020; Tek et al., 2021), resolution remains insufficient, and lithological information obtained from boreholes remains too sparse to comprehensively characterize the sedimentary character of channel-levee reservoir architecture (Stanbrook and Bentley, 2022). Consequently, comprehensive insights into the sedimentary heterogeneity and composition of discrete channel-levee architectural elements are lacking. In this context, well-exposed extensive outcrops are invaluable sources of information regarding the architecture of channelized turbidites and their bed-scale heterogeneity (Kane et al., 2007; Brunt et al., 2013; Morris, 2014; Hubbard et al., 2020; Kneller et al., 2020; Tek et al., 2020; Cunningham and Arnott, 2021; Reguzzi et al., 2023).

Although much work has been done to characterize outcropping channel fills, these are often of limited extent and lack detail to fully characterize channel fill across and along system, particularly into their correlative levees (cf. Pirmez and Imran, 2003; Kane et al., 2007; Vendettuoli et al., 2019; Reguzzi et al., 2023). As such, this study aims to provide a detailed outcrop characterization of a channel-levee complex to document the internal heterogeneity, and lateral and vertical stratigraphic evolution, of a well-exposed channel-levee complex. This complex (Complex 7 hereafter) is one of several superimposed channel-levee complexes belonging to the relatively fine-grained, sand-rich, Tachrift System, Taza Guercif Basin, NE Morocco (Fig. 1; Felletti et al., 2020, 2023). Complex 7 is approximately 30 meters thick and extends along a NW-SE-oriented continuous exposure of c. 2.5 km. Work focused on the northernmost outcrop of Complex 7, where a continuous 500-meter-wide transect, oriented approximately perpendicular to the paleoflow (N-NE), allows documentation of the facies, sedimentary units, and facies associations, which are the building blocks of the channel-levee complex; from the channel axis into the correlative overbank. Characterization of the sedimentology of this channel-levee complex permits reconstruction of the evolution from a meandering to sinuous channel system, with implications for the distribution of heterogeneity and connectivity of sandstone in channel-levee systems.

GEOLOGICAL SETTING

The Taza-Guercif Basin

The Taza-Guercif Basin (NE Morocco, Fig.1A) is a remnant, together with the Gharb and Fes-Meknes Basins, of the Rifian Corridor (Capella et al., 2018), an ancient seaway that connected the Atlantic Ocean with the Mediterranean Sea during the Late Miocene (Bernini et al., 2000; Gelati et al., 2000). The Taza-Guercif Basin (Fig.1B) originated in the early Tortonian due to the combination of the advancing thrust sheets of the Rifean system to the north and the strike-slip tectonics in the Middle Atlas chain (Bernini et al., 2000; Capella et al., 2018; Gelati et al., 2000; Sani et al., 2000; Capella et al., 2018). The basin overlies a Cretaceous to Early Miocene unconformity resulting from tectonic inversion of Jurassic rift faults of the Middle Atlas (Bernini et al., 2000; de Lamotte et al., 2009). The marine transgression in the basin began during the late Tortonian period, marked by sedimentation of the Ras el Ksar Formation, a shallow marine deposit up to 500 meters thick (Fig. 1C; Krijgsman et al., 1999).

Continued transgression led to the deposition of the Melloulou Formation, characterized by interbedded hemipelagic marlstones and turbidites, recording the basin-deepening and sedimentation rates during the Tortonian (Fig. 1C; Krijgsman et al., 1999; Bernini et al., 2000; Gelati et al., 2000; Sani et al., 2000). In the early Messinian, a tectonically controlled regression resulted in deposition of the Gypsiferous marlstones and the sand/mudstone alternation of the Kef Ed Deba Formation (Gelati et al., 2000; Sani et al., 2000). Continued uplift from 6.7 Ma resulted in termination of marine sedimentation (Krijgsman et al., 1999; Krijgsman and Langereis, 2000; Capella et al., 2018).

The Tachrift System

The Tachrift System, along with the El Rhirane System, constitutes one of the two turbiditic series in the Melloulou Formation, exposed to the east and west of the Zobzit River, respectively (Fig. 1B, C). The Tachrift System was mapped as nine vertically stacked channel-levee complexes (*sensu* Sprague et al., 2005; Felletti et al., 2020; 2023; Reguzzi et al., 2023; Zuffetti et al., 2023), each separated by meters-thick marlstones (Felletti et al., 2020, 2023). The Tachrift System spans a period of approximately 0.5 million years, dating from 7.7 to 7.2 million years ago (Krijgsman and Langereis, 2000).

The focus of this paper is the northernmost outcrop of channel-levee complex 7 (Fig. 1C) of the Tachrift System (Felletti et al., 2020). Interpretations suggest that these complexes represent the sequential deposits of channel systems originating from the south, evolving along a basinal slope dipping northward in the Taza-Guercif Basin (Gelati et al., 2000; Pratt et al., 2016).

Recent studies on the Tachrift System addressed the sedimentary architecture of selected parts of channel-levee complexes 4-6, describing laterally accreted deposits accumulated at bends of sinuous meandering channels as the dominant channel-filling element (Reguzzi et al., 2023; Zuffetti et al., 2023; Marini et al., this volume; Pantopoulos et al., this volume).

MATERIAL AND METHODS

The ca. 500-meter-wide part of outcrop belonging to Complex 7 (Fig. 2A), located in the northwesternmost area, was investigated through the acquisition of thirty-five detailed stratigraphic logs acquired along a section parallel to strike, roughly perpendicular to direction of depositional flow (Fig. 2B). To achieve high resolution and precision, the logs were measured at an average spacing of 25 meters and geolocated using a Garmin GPS. A high-precision Jacob's staff with a laser pointer (Patacci, 2016), clinometer, and compass allowed accurately rapid long-distance measurements, i.e., of mudstone-rich intervals.

Logs were described at centimeter resolution with particular attention paid to recording mud-clast frequency and composition, sedimentary structures, fossil fragments, trace-fossil type and intensity, and organic matter. Also, the bed-base character (linear, undulating, or erosional) and associated paleocurrent information were recorded.

Correlations between logs were traced physically by walking out beds and tracing beds in photo-panels. In the rare absence of lateral outcrop continuity, correlations were achieved by comparison of stratigraphic patterns and facies associations. Subsequently, logs were digitized enabling quantitative data extraction, including bed thickness, grain, etc., which was conducted utilizing EasyCore®.

Various parameters were computed from field data to explore the internal heterogeneity of the studied complex. These parameters are: i) proportion of sedimentary structures, ii) net-to-gross (hereafter, NTG), iii) amalgamation ratio, iv) mud-clast-horizon thickness percentage, v) mean and basal grain size, vi) and bed thickness.

Sedimentary-structure proportions were determined by calculating the percentage of observed thickness of sedimentary structures in a specific interval. In this work the NTG was computed as the ratio of total sandstone and conglomerate thickness to total stratigraphic thickness for each log (*sensu* Macdonald et al., 2011; Kus et al., 2022). The amalgamation ratio was defined as the ratio between the number of amalgamation surfaces and the total number of event beds in a given stratigraphic interval (*sensu* Romans et al., 2009; Kus et al., 2022). The mud-clast-horizon thickness percentage is expressed as the percentage of the cumulative mud-clast-layer thicknesses vs. the stratigraphic thickness of the studied unit, e.g., when stating mud-clasts reach 50%, this means that 50% of the unit thickness contain mud-clasts. For each log, grain-size data from the basal part of each bed and successive measurements at 1 mm intervals from the base to the top of each bed were utilized to calculate data on basal and mean grain size. Bed-thickness data were obtained by measuring sandstone and mudstone bed thicknesses with a resolution of 1 cm. Data plotting and analyses were conducted using Excel.

A deep-water "system", here the Tachrift System, refers to a succession of multiple channel complexes (*sensu* Sprague et al., 2005) separated by fine-grained sediment, here marlstones, and according to Mutti (1992) and Normark et al. (1993) represents an ancient turbidite system, that is, the fossil remains of an entire episode of clastic accumulation in the deep sea. As defined by Sprague et al. (2002), Campion (2005) and Sprague et al. (2005), discussed by Pickering and Cantalejo (2015), and utilized by earlier works in the Taza-Guercif Basin (Felletti et al., 2020, 2023; Reguzzi et al., 2023), the term "complex" is used to describe a high-level assemblage of multiple channel fills, bounded below and above by significant hemipelagic deposits; hence this term is appropriate for the channel complex studied here, since it refers to packages with a scale similar to that of Complex 7 (Fig. 2; Gardner and Borer, 2000; Sprague et al., 2005; Cullis et al., 2018). The term "Unit" refers to a stratigraphic unit, with variable thickness and represents deposition during a given phase of channel evolution, comparable to a channel fill of Sprague et al. (2005). A unit is composed of a few to several architectural elements, each of which may be the preserved product of deposition in one more seafloor channels and their overbank. Architectural elements are the interpreted depositional bodies related to deposition from different types of channelized and overspilling flows, e.g., erosional channel-fills, lateral accreting packages, levees etc. Hence, any unit may be composed of multiple architectural elements.

The term “channel” has no hierarchical implications and refers to a geomorphological element of the seafloor.

RESULTS

Complex 7 is here divided into five units based on physical correlations, facies, facies associations, and the hierarchical arrangement of major stratigraphic surfaces that can display erosional, depositional, or a combination of both features (Fig. 2B).

Sedimentary Facies

Ten distinct sedimentary facies were identified based on lithology, grain size, sedimentary structures, thicknesses, and the ratio of sandstone to mudstone (Fig. 3). Among these facies, three are chaotic deposits (f1a, f1b, and f1c), one is a poorly sorted conglomerate (f2), five facies consist of sandstones (f3 to f7), and one relates to mudstones (f8).

Sand-dominated chaotic (f1a)

Observations: Facies f1a consists of sand-rich chaotic deposits (Figs. 3, 4A) ranging in thickness from 0.5 to 1 meter. Clasts comprise plastically deformed sandstones and polygenic granules to cobbles of Jurassic carbonates and sandstones. In the sand-rich matrix, mud-clasts ranging in diameter from 1 to 5 centimeters and rounded polygenic extra clasts (granules and pebbles) are observed. The base is erosional, and the top is commonly capped by mudstones.

Process interpretation: Cohesive, plastic, laminar sand-dominated debris flows, with a mixture of exotic, but mainly reworked, clasts are supported by the cohesiveness of the flow (Lowe, 1982).

Mud-dominated chaotic (f1b)

Observations: Facies f1b consists of mud-rich structureless deposits with thickness ranging from 1.5 to 3 meters (Figs. 3, 4B). Mud clasts, polygenic granules to pebbles clasts, and biogenic fragments (shells and corals) are observed in the matrix. Decimetric boulders of well-cemented, very fine to fine sandstone are often immersed in the matrix. The bases are commonly erosional, and the tops of these deposits are always eroded.

Process interpretation: Deposition due to a cohesive, plastic, laminar mud-dominated debris flow (Lowe, 1982).

Debrites (f1c)

Observations: This facies consists of sand-rich to silt-rich mudstones, with thickness ranging from 0.1 to 0.5 meters (Fig. 3). Occasionally, wood, coal fragments, and extraclasts (granules) from Jurassic carbonates and sandstones are observed. These deposits are non-graded, typically extremely bioturbated, and oxidated. No other sedimentary structures are recognizable. The base is commonly erosional, and the top of these deposits usually show erosional features.

Process interpretation: En masse freezing of a cohesive debris flow. During deposition the grains of different sizes were not segregated by differential setting (Talling et al., 2012).

Poorly sorted conglomerate (f2)

Observations: Poorly sorted, clast-supported granule to pebble conglomerate (Figs. 3, 4C). This facies is found in a single horizon of variable thickness, up to 1 meter. Polygenic clasts from the Jurassic basement are typically well-rounded with high sphericity. Clast contacts are tangential and rarely linear. Clast sorting varies from well to poorly sorted moving away from log-section 28.5 (Fig. 2). Rare clast imbrication was recorded. Fossil fragments, including shells, as well as reworked corals, are noticeable. The base of this horizon shows erosional features. The top is normally eroded with preservation of rare thin mud-cap (a few centimeters).

Process interpretation: Traction-carpet sedimentation from a largely bypassing high-density turbidity current (Mutti and Normark, 1987).

Very thick-bedded massive amalgamated sandstone (f3)

Observations: Amalgamated sandstone beds of varying thicknesses, from 1 to 3 meters (Figs. 3, 4D). Consisting of coarse-to-medium to-coarse-grained, massive sandstones, normally grading to finer grain sizes towards the bed top. Inthese layers, coarse-grained lenses up to 0.5 meters thick, along with millimeter-scale (from 2 to 10 mm) traction-carpets were observed. Occasionally, reworked coral remains and shell fragments are observed. Beds often show mud-clast breccias near their erosional bases, and dispersed mud-clasts can be observed through the whole beds. The tops of these layers are frequently bioturbated.

Process interpretation: Rapid deposition from an unsteady but fully turbulent sand-rich high-density turbidity current (Lowe, 1982; Talling et al., 2012).

Thick-to medium-bedded amalgamated sandstones (f4)

Observations: The main differences between facies f4 and f5 is the thickness of the sandstone beds. F4 consists of medium-to coarse-grained sandstones, normally grading upwards to fine-grained sandstones, typically amalgamated, with a thickness ranging from 0.5 to 1.5 meters (Figs. 3, 4E). In coarse-grained intervals, bioclastic fragments are often observed. Mud-clast breccias are common near erosional bases. At the top of this facies, low-angle and planar-parallel millimetric-scale lamina are composed of coarser sandstones.

Process interpretation: Loss of capacity, along with a lack of flow steadiness, of a medium-density turbidity current allowed deposition of this facies (Lowe, 1982; Mulder and Alexander, 2001).

Medium-bedded structured sandstones (f5)

Observations: This facies consists of medium-coarse to fine sandstones, typically graded, with a thickness ranging from 0.15 to 0.5 meters (Fig. 4F). This facies is characterized by planar parallel and low-angle lamina usually observed at the base and towards the middle of the beds. The bases of the beds show erosional features and may display sole marks, such as flute and groove marks. Usually, near the top of the bed, millimeter-scale mud-clasts, pervasive bioturbation, oxidation, and fragments of oxidized wood are observed. Beds often tend to split and amalgamate laterally. Overlying the sandstone part of beds a mud-cap of maximum 20 cm in thickness is often present.

Process interpretation: Waning, low- to high-density turbidity currents (Lowe, 1982; Li et al., 2016).

Thin-bedded laminated sand-mud couplets (f6)

Observations: Facies f6 is composed of medium-to-fine to very-fine sandstones, with bed thickness ranging from 0.05 to 0.2 meters (Fig. 4G). Planar-parallel lamination is common and usually oxidized. These beds are normally separated by thin (0.01 to 0.05 m), bioturbated mud caps; rare amalgamations are observed. Bases are sharp, flat, and depositional. Ripples are rarely observed at the top of beds.

Process interpretation: Low-density waning flow (Lowe, 1982).

Very thin-bedded sand-mud couplets (f7)

Observations: Facies f7 is composed of fine to very-fine sandstones, ranging from 0.02 to 0.1 meters thick (Figs. 3, 4H). Sandstones are capped by a bioturbated mud-cap 0.02-0.1 meters thick. Rarely, these sandstones beds are characterized by planar-parallel lamination, and bioturbation is often present, affecting the entire bed thickness. Beds are often oxidized. Beds bases and tops are sharp, flat, and parallel.

Process interpretation: Slow deposition from low-density turbidity currents (Lowe, 1982; Mulder and Alexander, 2001).

Marlstone (f8)

Observations: Facies f8, is composed of gray, massive, non-gradedcalcareous mudstone in packages ranging in thickness from a minimum of 0.01 meters to a maximum of 10 meters (Fig. 3). Locally it contains fossils fragments, bioturbation, and oxidized layers.

Process interpretation: Hemipelagic background sedimentation and deposition from the least concentrated part of a low-density turbidity current (Mutti, 1992).

Sedimentary Facies Association

Six distinct facies associations (FAs) have been identified and grouped in three categories based on their distinct depositional styles: 1) erosional channel-fill elements (FA1 and FA2, Figs. 5 A, B); 2) laterally accreting elements (FA3, FA4, and FA5, Figs. 5A, C); 3) and overbank elements (FA6, Figs. 5A).

Erosional channel-fill elements

FA1: Channel axis

Observation: FA1 is characterized by thick sandstone bedsets and chaotic deposits (facies f3 and f1a, f1b; Figs. 5A, B, 6). The sandstones have variable thickness ranging from 1 meter to approximately 3 meters with a NTG of 100% (Fig. 5A). The sandstone bedsets exhibit erosional bases showing a high presence of mud-clast breccias (f3; Fig. 5A). The amalgamation rate is 100% (Fig. 5A).

The chaotic deposits (facies f1a; Figs. 7A, B, C) have variable thickness ranging from 1 to 2 meters and erosional bases. Inside these deposits, sandy rafts, fossil fragments, and pebbles in muddy matrix are frequently found.
FA1 is observed in the central part of the studied transect in between logs 32 and 40 (Fig. 6).

Interpretation: The presence of chaotic deposits and thick amalgamated sandstones, combined with the absence of thinner-bedded facies and gently dipping erosional surfaces that could represent lateral migration, suggests that deposition was largely from the basal parts of mainly bypassing, erosive, high-density flows in the channel axis. Such flows are unlikely to construct highly sinuous channel fills; rather, they are interpreted as fill of a relatively straight erosional channel (e.g., Camacho et al., 2002; Fildani et al., 2013).

FA2: Channel margin

Observation: FA2 is characterized by sandstone bedsets (facies f3, f4 and f5; Figs. 5A, B, 6, 7A, D) with variable thickness, from 0.3 to 1.5 meters and an amalgamation ratio ranging from 90 to 100% (Figs. 5A, B). NTG ranges between 80% and 100% (Figs. 5A, B). Contacts are typically erosional. The main facies in this association are f3 and f4, with sporadic debrites (f1c). At the top of this facies association, fine-to medium-grained beds from facies f5 can be observed.
FA2 can be observed in logs 32 and 28 to the western side of the channel (Fig. 6). To the eastern flank, FA2 is observed from logs 39 to 45.5 (Fig. 6).

Interpretation: The less amalgamated configuration of this association is interpreted as the deposition at the channel margin of a confined channel and may be related to a gradual filling of the erosional channel (FA1) and a consequent spill-out of the flow (e.g., Camacho et al., 2002; Fildani et al., 2013; Hubbard et al., 2014).

Laterally accreting elements

These elements show a sigmoidal geometry in cross-sectional view, roughly perpendicular to the main paleoflow direction, towards the north (Figs. 6, 7E). Differences in facies distribution, NTG, basal grain size, and amalgamation rate help in recognizing three facies associations (FA3, FA4, and FA5; Fig. 5A) representing different part of a sigmoid (Fig. 5C).

FA3: Top-set

Observation: FA3 is characterized by fine to medium sandstone bedsets with a variable thickness ranging from 0.2 meter to 1 meter in logs 20 and 26 (log 18, Figs. 5C, 6, 7E, C). Sandstone bases are predominantly depositional, with sporadic erosional surfaces. The basal grain size ranges from medium to fine. Thin sandstone beds are intercalated with bioturbated mudcaps of similar thickness (facies f6 and f7; Fig. 7F). The NTG and the amalgamation ratio range between 30% and 40% (Fig. 5A). Occasionally, corresponding with erosional basal surfaces, debrites (f1c), up to 50 cm thick, are observed.

This FA3 is present between logs 17 and 30 in the western sector and between logs 39 and 49 in the eastern sector (Fig. 6).

Interpretation: FA3 is interpreted as the top-set, the region of the laterally accreted sigmoid that lays above the inner bank (*sensu* Abreu et al., 2003; Li et al., 2018; Arnott et al., 2021; Reguzzi et al., 2023).

FA4: Middle-set

Observation: FA4 comprises facies f3, f4, and occasionally at the top the thin-bedded f5 (Figs. 5A, C, 7E). This association consists of amalgamated sandstone bedsets with a variable thickness ranging from 0.15 meters to 1.5 meters. Typically, the sandstones are normally graded, with basal grain sizes ranging from coarse to fine sand (Fig. 5 A-C). The NTG ranges between 80% and 100%, and the amalgamation rate ranges between 80% and 100% (Fig. 5A). The bases of sandstone bedsets are mostly erosional. Near these bases, thin conglomeratic horizons (f2) are rarely observed. Sedimentary structures in this association are dominated by parallel and low-angle lamina. This FA is observed along the whole studied transect (Fig. 6).

Interpretation: The thick, amalgamated sandstone bedsets are interpreted as the middle part (middle-set) of the sigmoid, representing lateral accretion of the channel (*sensu* Abreu et al., 2003; Li et al., 2018; Arnott et al., 2021; Reguzzi et al., 2023).

FA5: Toe-set

Observation: FA5 comprises amalgamated sandstones with a thickness ranging from 0.3 to 1.5 meters (Fig. 5 A-C). The thickness of the layers is influenced by frequent erosional surfaces in this facies association. Sandstones vary from medium to coarse, and the beds are typically normally graded (Fig. 5 A-C). The NTG and the amalgamation ratio range between 90 and 100% (Fig. 5 A-C). The main facies of this association is f4 with local poorly sorted conglomerates of f2 (Fig. 7G-H). This FA is observed between logs 30 and 28 and from logs 26 to 24 (Fig. 6). Higher in the stratigraphy it is observed between logs 27 and 33 and from logs 35 to 46 (Fig. 6).

Interpretation: this FA is interpreted as the toe-set, representing the downlap termination of the sigmoid (*sensu* Abreu et al., 2003; Li et al., 2018; Arnott et al., 2021; Reguzzi et al., 2023).

These FA 3-5 usually are larger than the erosional channel-fill elements, with thickness in the range of 1 to 2.5 meters and widths of ca. 300 meters. These sigmoidal elements record the incremental deposition in the inner bank during the migration of the channel and can be interpreted as lateral accretion packages (LAPs; *sensu* Abreu et al., 2003; Hubbard et al., 2009; Li et al., 2018; Arnott et al., 2021; Reguzzi et al., 2023)

Overbank elements

FA6: Overbank (levee/terrace)

Observation: FA6 comprises alternations of sandstone and mudstone layers (f6 and f7) with thickness ranging from 0.01 to 0.2 meters, with a NTG ranging from 20 to 30% and an amalgamation ratio of 0-20% (Figs. 5A, 6). The basal grain size varies from fine to very fine (Fig. 5A).

FA6 crops out between logs 17 and 30 on the western flank of the channel and between logs 45.5 and 49 to the eastern flank (Fig. 6). This FA is observed in the lower part of the stratigraphy between logs 17 and 30, to the west of the channel occurs between logs 17 and 32, east of the channel between logs 45 and 49 and in the upper part this FA is observed along the whole transect (Fig. 6).

Interpretation: This FA is interpreted as overbank deposits formed due to overspill of the upper, low-density part of turbidity currents passing through adjacent channels and forms the levee to Complex 7 (*sensu* Piper et al., 1999; McHargue et al., 2011; Li et al., 2018; Reguzzi et al., 2023). Although these are likely levees, with no larger-scale confinement identified, they may also represent terraces (e.g., Hansen et al., 2017).

Stratigraphic Framework

Based upon the facies and correlation across thirty-five sedimentary logs, the stratigraphic framework can be divided into five units (1A, 1B, 2B, 2C, and 3; Fig. 8), each separated by basal erosional and/or depositional surfaces (S1-S2-S3-S4-S5, Fig. 8). Beds and packages of beds can be correlated tens of meters laterally (Fig. 8). The main characteristics of each unit are outlined below, from the lowermost unit to the top of the complex. Statistics were computed for key sedimentological variables (sedimentary structures, NTG, amalgamation %, mudclast horizons %, bed basal grain size, bed mean grain size, sandstone thickness, and mudstone thickness) for each sedimentary log and are then plotted by unit. The results of the statistical analysis enabled quantification of stratigraphic trends and differences between the units.

Unit 2A (Fig. 2) is not described in this paper, because its deposits are not documented in the transect of Complex 7 analyzed here.

Unit 1A

Observations: Unit 1A overlies a 10-m-thick interval of hemipelagic marlstones that separates Complex 7 from the underlying Complex 6 (Figs. 8, 9A, 10A). This unit has a thickness ranging from a minimum of 4.6 meters (log 19) to a maximum of 5.9 meters (log 22). In general, the thickness of the unit remains constant across the entire transect, although a slight reduction in thickness is observed moving eastward toward log 30 (Fig. 8). This unit is characterized by a vertical stacking of four small-scale (about 200 meters wide) lenticular bodies, consisting of amalgamated sandstone beds (facies f3 and f4; Fig. 9A and 9B) with a thickness ranging from 20 cm (log 20; Fig. 10A) to approximately 2 meters (log 17; Fig. 10A). Thin-bedded heterolithic intervals (facies f6 and f7, Fig. 9C, D, E) are intercalated within the amalgamated sandstone layers (Fig. 9B, C). The thin-bedded heterolithic intervals show a variable thickness ranging from 30 to 90 cm and an average NTG of 20%.

Massive sandstone is the most common structure in this unit, with an abundance of ca. 60% and a general decreasing trend from the west to the east (Fig. 10B). In contrast, the thin beds show an increase toward the east, from log 17 to log 30 (Fig. 10B). The NTG (Fig. 10B) remains relatively constant (c. 70%) along the entire transect. In log 28, there is a minimum of 60%, while the maximum NTG is observed in log 28.5 at 80%. The amalgamation rate remains stable along the studied transect (between logs 17 and 31) with values between 20% and 40% in this unit (Fig. 10B). Higher values (c.a. 35%) are observed in logs 19 and 22, and lower value (ca. 15%) in log 28. Mud-clast-horizon percentage exhibits low values (less than 10%), coupled with a trend of low values of amalgamation and NTG (Fig. 10B). The mean grain size of beds shows a clustering around 0.2 mm, with few outliers reaching 0.6 mm and 0.8 mm in logs 22 and 24 respectively (Fig. 10C). The basal grain size is always slightly larger than the mean grain size of the bed (indicating normal grading), and shows a slightly decreasing trend, from 0.4 mm in log 17, to 0.2 mm in log 22. To the east of log 22 the trend is more stable.

Although layers up to 1 meter thick were observed, the average thickness of sandstone beds (c. 10 cm) is consistently greater than that of intercalated mudstones, with a higher dispersion of values towards the West (Fig. 10D). The mean thickness of mudstone intervals is ca. 5 cm, with a stable trend for the studied transect (Fig. 10D). The apparently stationary sand-thickness distribution reflects the tabularity of sandstone and mudstone beds at the scale of the transect with no particular changes in the vertical stacking of the Unit (Fig. 10D).

Interpretations: The stable trend of the three mentioned parameters (Fig. 10B) is likely related to the development of small-scale channels that migrated laterally toward the east and aggraded vertically, separated by intervals with thin-bedded layers. Such small-scale channels have been recorded in the basal interval of other channel complexes in this system (Reguzzi et al., 2023; Marini et al., this volume; Pantopoulos et al., this volume). Another hypothesis is that these deposits could be related to distributary channels of frontal splays (e.g., Posamentier and Kolla, 2003).

Unit 1B

Observations: Unit 1B is bounded below by the surface S2 and above by S3 (Figs. 8, 9A). The thickness of this unit ranges from 8.30 meters (log 46; Fig. 8A) to 1.70 meters (log 33; Fig. 11A). The unit is characterized by sigmoidal-shaped amalgamated sandstones, laterally stacked with inclined bedding towards northeast (with an angle of c. 45° to the average paleocurrent direction, directed northward; Figs. 11A, 9A). Several changes in thickness, facies, and grain size are observed across a sigmoid. Usually, the bathymetrically elevated part of the sigmoid (FA3, top-set) is characterized by thin-bedded, fine-grained (facies f6 and f7), heterolithic intervals (ca. 80 centimeter in thickness in log 7), with NTG ranging from 0 to 20% (Fig. 11A). The middle part (ca. 2 meters in thickness in log 24) of the sigmoid (FA4, middle-set) is composed of thick, amalgamated sandstone beds (facies f3, f4) displaying a NTG of 80-100% and an amalgamation ratio ranging between 80 and 100% (Figs. 9A, 9B). The bathymetrically lowest part of the sigmoid (1 meter thick in log 28.5; FA5, toe-set) shows erosional features and is composed of amalgamated sandstone beds (f4) with conglomeratic basal lags (f2) and chaotic deposits (f1c); the NTG is 90 to 100% and the amalgamation percentage is 90-100%. The percentage of mud-clast horizons is around 20%, concentrated primarily at the base of the middle part of the sigmoid.

The most common sedimentary structure in Unit 1B is massive sandstone, with a mean abundance of 70% in the whole studied transect (Fig. 11B). The only exception is in log 28.5, where the value of massive sandstone is c. 20%, coupled with an increase in chaotic levels up to 40% of this unit (f1c) and coarser grain sizes (conglomeratic basal lags; f2). This behavior can be explained by considering that this log samples a sigmoidal structure in its lower part (FA5, toe-set). Thin-bedded intervals (f6-f7) have lower values with respect to Unit 1A, never reaching 20%. In logs 21, 28, 44, 46, and 47 the thin-bedded abundance is 0%, suggesting the hypothesis that these logs intersect a sigmoid exclusively in its middle and basal parts.

The NTG (Fig. 11B) is stationary along the transect at c. 90% with the exception of log 38, where the NTG reaches the 100%, although between logs 19 and 23 NTG decreases to c. 80% as the upper part of some sigmoidal structures (top-set) is partially intersected. The percentage of amalgamation varies from 40% in log 17 to 100% in log 38. This behaviour can be explained by considering that individual logs intersect different parts of sigmoidal structures (i.e., top-set, middle-set, and toe-set) that are juxtaposed vertically and horizontally. Similar behavior is observed for the percentage of mud-clast horizons, where the values range between 10 and 40% for this unit (log 24; Fig. 11B).

The mean grain size shows a stationary trend with few variations fluctuating around 0.2 and 0.5 mm; all along the studied transect (Fig. 11C). Few beds have grain sizes reaching 5 to 7 mm, those that do are observed in logs 26, 27, and 28.5, which represent the basal lags of the sigmoidal structures. The basal grain sizes, when compared to the average values of the beds, are higher (around 0.5 mm) and with less dispersion (Fig. 11C), indicating normal grading in beds; higher values are observed in logs 26 (9.5 mm) and 28.5 (6.0 mm), which represents the conglomeratic basal lag (f2) at the base of the sigmoidal structures (FA 5 – Toe-set).

The average thickness of the sandstones is around 20 cm, with a wide dispersion reaching up to 1.40 m in log 38 (Fig. 11D). These relatively high values of sandstones thickness are accompanied by low thicknesses of the muddy division, averaging around 10 cm (Fig. 11D).

The similarity in the plots in Figure 11B reflects the configuration of the Unit 1B, usually composed of thick, vertically stacked sandstones. Slight differences are observed between the western and the eastern part of the outcrop. The higher values in the eastern sector (between logs 38 and 47) are explained by the decrease of thin-bedded heterolithic facies and the predominance of massive sandstones.

Interpretations: Outcrop observations supported by statistical analysis point to Unit 1B as the result of progressive lateral expansion and migration towards the east. This is approximately perpendicular to the average paleocurrent direction and is interpreted as the result of meandering channels, producing groups of sigmoidal-shaped beds (LAPs, lateral accretion packages; *sensu* Abreu et al., 2003; Arnott, 2007; Li et al., 2018).

Unit 2B

Observations: Unit 2B is bounded by two surfaces, S3 and S4 (Figs. 8, 9A). Surface S3 shows erosional features from logs 28.5 to 47 (Fig. 12A), while in its westernmost part (between logs 17 and 28.5) the surface can be considered depositional (Figs. 8, 13A). Similarly, surface S4 can be considered erosional at the scale of the logged transect, except for its westernmost part (from log 17 to log 24). The minimum thickness of this unit is documented in log 20 (1.0 meter), while its maximum thickness, 3.0 meters, is recorded in log 45. In an east-west orientation, perpendicular to the average paleocurrent direction, the unit shows a symmetrical channelized geometry (FA1 – Channel axis), with a deep incision (10 meters) between logs 28 and 40 and the flanks more gently ascending towards log 17 to the west and log 49 to the east (Fig. 12A). At the point of deepest incision, between logs 33 and 37, the unit is characterized by chaotic deposits (facies f1a and f1b; Fig 12B) ranging in thickness between 0.5 to 2.0 meters. West of the central part of the incision (between logs 29 and 32), thick layers of amalgamated sandstones are observed (facies f3 and f4; Fig. 12C), gradually pinching out with onlap geometries (Fig. 12D and 12E). Farther to the west (from log 28.5 to 17; Fig. 12F), the unit is characterized by heterolithic thin beds belonging to facies f6 and f7 (Fig. 12F). Similar characteristics are observed to the east of the deepest incision, where thick amalgamated sandstones (from log 37 to 49, facies f3 and f4; Fig. 12G) gradually transition to and alternate with heterolithic intervals (Fig. 12G). The thin beds exhibit relatively high proportions of this unit (Fig. 13B) on both the west (around the 50% between logs 19 and 28.5) and east sides (60% towards log 48) of the incision, while in the central part of the transect these decrease, reaching 0% in log 32. The NTG % and amalgamation % illustrate this pattern (Fig. 13B). In the central incisional area (log 38), values of NTG % and amalgamation % are near 100% and gradually decrease towards lateral positions (0% NTG and amalgamation towards the west in log 19, and 50% NTG and 0% amalgamation at log 48 towards the east, which seems more sand prone; Fig. 13B). The percentage of mud-clast horizons consistently remains below 10% of the unit. Only in the most axial zones of the incision does mud-clast content increase, reaching up to 80% of the thickness of this unit in log 38 (Fig. 13B). The mean and basal grain size of beds (Fig. 13C) show a clear trend that becomes coarser (0.6 mm in log 38) and more dispersed towards the center of the incision and decreases symmetrically towards both sides of the incision (0.2 mm in log 19 and log 48).

As with the other statistics (Fig. 13D), the thickness of the sandstones shows higher medians (max value of 35 cm in log 38) and dispersion at the center of the incision, progressively decreasing towards the more marginal areas (2.0 cm in log 19 and 48). The presence of thick, amalgamated sandstone layers (which can reach up to 70 cm in thickness) is highlighted by the widened dispersion of the boxplots in the central part of the transect, which also correspond to a minimum thickness of the mudstone layers (median value around 2.0 cm between logs 38 and 32; Fig. 13D).

Interpretations: The sedimentological characteristics are the result of persistent erosion into the pre-existing sandstone of Unit 1B. Here, parts of the transiting flows were deposited in its central and erosional parts (FA1, thick amalgamated layers, coarser and widely dispersed grain sizes, abundance of mud clasts). Away from the axial zone, there is a facies transition towards thinner and finer layers, which represent the margins of the channel (FA 2, Channel margin).

Unit 2C

Observations: Unit 2C is bounded by two main surfaces (S4 and S5) that exhibit erosional characteristics along almost the entire length of the transect, oriented orthogonally to the average paleocurrent direction (Fig. 8; 12A). Significant basal erosion (S4) is discernible between logs 31 and 40, where the unit achieves a maximum thickness of 6.4 meters at log 34 (Fig. 11A). This deep incision diminishes in depth towards the eastern and western end of the transect (Fig. 8 and 14A). To the east of log 45, the unit is no longer present due to erosion by the Unit 3 (Fig. 12G).

Unit 2C is characterized by the presence of thick amalgamated sandstone beds (f3; logs 31 to 40) in its thickest part, showing onlap terminations (Fig. 12A). The complex geometries of these layers are the result of erosion consistently occurring at the bases and tops of these beds (Figs. 8, 14A). Chaotic levels are present at the base of the unit, from log 38 to log 45, reaching 25% of the thickness of the unit thickness. Conversely, the upper part of the unit exhibits a well-developed transition from thick and amalgamated beds to gradually thinner heterolithic intervals (f6 and f7 in logs 17 to 27).

The relative proportion of thin-bedded heterolithics decreases toward the axial part from 70% in log 19, to 0% in log 31 (Fig. 11B). In the same part of the transect, this trend correlates with an increase of: i) massive sandstones from 50% in log 20 to 100% in log 36 (Fig. 14B); ii) massive sandstone with traction-carpets (maximum frequency -30%; Fig. 14B);

iii) NTG % (from 15% in log 19 to 100% in between log 32 and 44; Fig. 14B); iv) amalgamation % (value rapidly increases from 0% to above 80% between logs 31 and 44; Fig. 14B); v) the median of the mean grain size of the beds, increasing from 0.2 mm between logs 19 and 25 to a maximum value of 0.5 mm in log 33 (some outliers reaching values of 1.2 mm and 0.9 mm are observed in logs 27 and 34 respectively; Fig. 14C); and vi) basal grain size (maximum values are around 0.7 mm recorded in between logs 32 and 35; Fig. 14C). Outlier values in basal grain size are observed in logs 26 and 42, ca. 1.2 mm and 1.3 mm, respectively (Fig. 14C). The percentage of mud-clast horizons reaches its highest values (around 60%) toward the marginal parts of the incision (log 30 and log 41), while having lower values (around 20%) in its more axial parts (Fig. 14B).

Sandstone-thickness distribution shows a symmetrical trend with respect to the axis of the main incision (Fig. 14D). Bed-thickness plots show low values and low dispersion (less than 25 cm) between logs 19 and 30. Values increase abruptly (up to 1.0 m) between logs 31 and log 39, where there is greater range of values, which can exceed 2.5 meters in thickness. The median thickness of mudstone intervals consistently has values below 20 cm, associated with a very low range of values (Fig. 14D).

Interpretations: Unit 2C represents multiphase infill of a channel, which eroded the underlying Unit 2B. In its initial stages of development, the flows were mainly contained within the channel. Subsequently, there is evidence of gradual filling and consequent lateral expansion, leading to the formation of overbank deposits, preserved on the western margin.

Unit 3

Observations: Unit 3 lies above the erosional surface S5 (Figs. 8, 12A). The top of the unit is represented by a thin sandstone, which is laterally correlated along the entire transect, capping Complex 7. Above this, deposition is exclusively characterized by thick marls (f8) interspersed with thin-bedded turbidites. The thickness of Unit 3 ranges from 0.4 (log 17) to

2.8 meters in log 32 (Fig. 15A). The greatest thickness occurs where surface S5 eroded the underlying Unit 2C most extensively, between logs 28 and 49 (Fig. 15G). Correlation shows that this incision is filled by thick beds of amalgamated sandstones with erosional bases and truncated tops (facies f3 and f4; Figs. 8, 12A, F, G), which can reach up to 80% of the thickness of this unit, as observed in log 42. In some cases, they exhibit sigmoidal geometries, dipping towards the east (Figs. 12F, G, 15A). An eastward migration of these sigmoids is commonly observed. Chaotic facies are observed above erosional surfaces from log 40 to 49, with percentages of the thickness of chaotics fluctuating between 10 and 20%, with a maximum of 50% of the thickness of this unit in log 45 (Fig. 15B).

Thin-bedded heterolithics (f6 and f7; Fig. 15G) are present in various stratigraphic levels in the whole transect, with the percentage of their thickness fluctuating around 10 to 20% of the unit, except for log 28 and 45, where the value is around 50% of the thickness of this unit (Fig. 15B).

NTG, amalgamation % and mud-clast-horizon thickness % remain high, with significant variations and without any apparent trend (Fig. 15B). NTG shows some fluctuation above the 60%, with a minimum value in log 39 (c. 60%) and a maximum value of c. 95% in logs 47 and 49 (Fig. 15B). Minimum amalgamation values (10%) are in logs 35 and 36 and rapidly increase from 15% to 90% in logs 45 and 49 (Fig. 15B). The mud-clast-horizon thickness % ranges between 10% and 30% along the studied transect (Fig. 15B). Minimum values (0%) are recorded in logs 27 and 28, while the maximum (40%) is recorded in log 49 (Fig. 15B). The high range of these three variables across the transect, without any recognizable trend, can be explained by considering that subsequent logs sample different positions of laterally accreted small-scale elements (Fig. 15B).

The same reasoning, of sampling different parts of LAPs, can be extended if we consider the grain size (Fig. 15C) and bed thickness (Fig. 15D). The median value of the mean grain size remains constant around 0.2-0.3 mm along the whole transect, although its variability is high. A few outliers above 1.3 mm are measured in logs 35 and 45.5. The basal grain size is consistently larger than the mean grain size of the bed and clusters around 0.4 mm (Fig. 15C). Outliers reaching 1.5 mm and 2 mm are observed between logs 31 and 37.

The median of sandstone thickness remains around 10 cm and is consistently greater than the thickness of mudstone intervals (ca. 5 cm). The higher values are noted between logs 31 and 40. Outliers, with values exceeding 80 cm, are observed in logs 29 and 34.

Interpretations: Unit 3 represents the result of progressive lateral expansion and migration towards the east, approximately perpendicular to the average paleocurrent direction of meandering channels, producing groups of sigmoidal-shaped beds (LAPs) similarly to other documented channel fills (e.g., Jobe et al., 2010). This last phase of channel construction restored the depositional style observed in Unit 1B. Following this unit, a sharp deactivation of the complex occurred, representing either abandonment or avulsion of the channel.

DISCUSSION

Spatio-Temporal Evolution of the Channel-Levee Complex

This study presents a detailed characterization of the sedimentary fill of an exceptionally exposed channel-levee complex, which allows a reconstruction of its spatio-temporal evolution, from inception to abandonment (Fig. 16). The stratigraphic evolution of Complex 7 can be subdivided into three phases corresponding to the main evolutionary steps of complex 7, with each phase being the timespan of the broad units, i.e., Phase 1 = Unit 1A and 1B, Phase 2 = Unit 2B and 2C, and Phase 3 = Unit 3

The channel dimensions described here refer exclusively to the preserved and outcropping parts of channel fills, which were generated by multiple seafloor channels. However, these channel-fill dimensions do not correspond to the dimensions of the individual channels that constructed them, with seafloor channels representing only fleeting images of transient, often erosional, and as such the compound and partial remnants of geomorphic channels.

Phase 1

This phase represents the initiation of deposition of the channel complex, directly overlying a 10-meter-thick marlstone interval that separates Complex 7 from the underlying channel-levee complex 6 (Fig. 16A; Zuffetti et al., 2023). Phase 1 is marked by the presence of relatively thin channelized sandstone deposits (0.1 to 0.6 meters thick, tens of meters wide) belonging to Unit 1A, intercalated with mudstones (up to 0.8 meters thick). These channel fills are thought to represent a narrow, sinuous and meandering channel migrating towards the E.

These small-scale channel fills ca. 200 meters wide and 1-meter-thick, may represent a gradual initiation of the system, with through-going channels, recording the first channel activity within the complex, propagating through the area during a time of sedimentation characterized by waxing flow (e.g., McHargue et al., 2011). A similar initiation was documented by Reguzzi et al. (2023).

After Unit 1A, Unit 1B represents the result of progressive lateral expansion towards the SSE during Phase 1. Unit 1B deposits are interpreted to represent LAPs formed channels larger than those of the Unit 1A. Ongoing deposition in the inner bank and subsequent erosion of the outer bank, accompanied by overspilling at correlative levees, documents channel migration towards the SSE, approximately perpendicular to the main paleoflow direction (Fig. 16B).

The spatial arrangement of these laterally migrating channels implies an increase in sediment supply when compared to Unit 1A. The increasing sediment flux was likely constant to generate and maintain a meandering channel (*sensu* at grade channels of Abreu et al., 2003; Kneller, 2003).

Similar deposits resulting from meandering channels are well-documented in both outcrop (e.g., Abreu et al., 2003; Arnott et al., 2021; Li et al., 2018) and subsurface (e.g., Janocko et al., 2013; Reimchen et al., 2016) investigations. They are generally characterized by gently dipping, sigmoidal-like sandstone beds with erosional bases, formed by a variety of flow processes involving flow separation, bed-load transport, and waning-stage suspended-load fallout (Dykstra and Kneller, 2009), which laterally migrate in a channel in a fashion similar to fluvial point bars (Abreu et al., 2003; Arnott, 2007; Dykstra and Kneller, 2009). A variety of evolutionary models have been proposed regarding infilling of laterally migrating channels, highlighting the importance of autogenic and allogenic factors such as channel avulsion, tectonics, sediment supply, channel confinement etc. (Hubbard et al., 2008; Hansen et al., 2015). Based on the aforementioned evolutionary models, the presence of a number of channel-fill and overbank architectural elements have been proposed associated with channelized features ranging in scale from individual channel-fill elements to channel complexes. Such architectural elements represent either smaller-scale channel fills, terraces, or internal levees constructed within the channel or external levees and splays beyond the channel (Hansen et al., 2015; Hansen et al., 2017). Other proposed models favor the effects of punctuated lateral incision and bench formation at the inner bank of the thalweg instead of lateral point-bar-like migration for the infilling of laterally migrating channels (e.g., Maier et al., 2012).

Phase 2

The youngest stage of this phase (Unit 2A; Fig. 2) is not described in this paper since their deposits are not documented in the transect of Complex 7 analyzed here.

Phase 2, corresponding to units 2B and 2C, is marked by a significant change in depositional style from the meandering channels of phase 1 to an erosionally confined channel-fill, the base of which is marked by a chaotic mass-transport deposit (Fig. 16C). In this context, parts of the channel-transiting flows were deposited in the central part of the thalweg, which is characterized by thick amalgamated and mud-clast rich sandstones with relatively coarse grain size. Away from the thalweg, there is a facies transition towards thinner and finer layers, representing the marginal deposits of the channel fill. Channel margins pass to inner-levee deposits laterally away from the channel fill, presumably generated by the overspill of the upper part of the flows in the main channel area (e.g., Hansen et al., 2015).

These deposits, belonging to Unit 2B, may represent the infill of the last open channel of the meandering channel phase (e.g., Janocko et al., 2013). However, continued lateral migration to the SSE is documented during the previous phase (1, Unit 1B), before a distinct switch in the focus of channelized flow back towards the NNW in Phase 2, with cutting of an erosional channel into the pre-existing deposits. As such, Phase 2 represents an erosionally confined channel-fill type entrenched into older meandering channel fills (Fig. 16C, e.g., Campion et al., 2000; Cronin et al., 2000). This shift could be attributed to both allocyclic (e.g., increased sediment supply, base-level fall, tectonic activity) or autocyclic (e.g., channel avulsion) controls.

The transition from channel-axis to channel-margin facies documented by Unit 2B shows similarity with the transition between channel axis and channel margin in the Cretaceous Tres Pasos Formation slope system proposed by Macauley and Hubbard (2013), where transition records axis to off-axis channel flows, with the axis dominated by bypassing flows (e.g., Hubbard et al., 2014), with deposition concentrated at the channel margins (e.g., Hubbard et al., 2020).

The upper part of Phase 2 is characterized by a more rapid filling of the channel, which had eroded into the Unit 2B. In its early stages, flows were predominantly contained within pre-existing erosional confinement created from Unit 2B deposition (Fig. 16D). Subsequently, there is clear evidence of more gradual infilling by thick and amalgamated sandstone beds, belonging to Unit 2C, of the pre-existing topography produced by both erosion and build-up of the margin during bypass (Hubbard et al., 2014). As accommodation decreased, flows started to overspill and allowed consequent lateral expansion, resulting in formation of channel margins and levees. The incremental filling of the channel could be related to a decrease in flow energy, resulting in deposition instead of bypass.

Subsurface data from seismic profiles of turbidite channels in the Niger Delta continental slope (Liu et al., 2013), record a channelized stratigraphic organization which is similar to that represented by Unit 2C sediments.

Phase 3

The confined deposition represented by the later stage of Phase 2 was interrupted by further channel erosion, as recorded by lateral accretion packages of a newly formed meandering channel migrating towards the SSE (Unit 3; Fig. 16E).

This final phase of channel evolution restored the depositional style observed in the late stage of Phase 1 (Unit 1B). The return to a depositional style characterized by laterally migrating channels could be a result of a reducing accommodation, coupled with an occurrence of a period of steadiness in the equilibrium profile (*sensu* Kneller, 2003).

In the upper stratigraphic levels of the complex, a transition into thin-bedded turbidites is recorded which might be related to deactivation or avulsion phase of the channel system.

Implications for the Distribution and Connectivity of Sandstone in Channel-Levee Systems

Hydrocarbon production from subsurface reservoirs belonging to deep-marine channel-levee complexes has increased during the last decades (e.g., Aniekwena et al., 2003; Godo, 2006; Shao et al., 2024), demonstrating their importance not only for hydrocarbons but also as valuable assets for CO_2 sequestration and underground gas storage (Weimer et al., 2000; Pettingill and Weimer, 2002; Abreu et al., 2003; Weimer and Pettingill, 2007; Marshall et al., 2016). Hence, a reduction of uncertainty and reliable estimation of reservoir quality and connectivity is crucial for maximizing production in channel-levee reservoirs characterized by complex vertical and lateral juxtaposition of a large variety of thick-bedded, coarse-grained vs. thin-bedded, fine-grained facies (e.g., channel, channel margin, to overbank deposits). The complex architecture and stacking pattern described from Tachrift Complex 7 can be used as a general guide for the estimation of reservoir characteristics (NTG, facies, connectivity) in similar relatively fine-grained, sand-rich, deep-water slope channel-levee reservoirs and their specific architectural elements (Alpak et al., 2013; Zhang et al., 2017; Jackson et al., 2019).

The observed architectural framework of Complex 7 arose from the evolution of initially isolated channels, through meandering to sinuous channels, interrupted by a phase of erosionally confined deposits, before re-establishment of meandering channels before abandonment. The result is the vertical and lateral juxtaposition of various depositional elements, including erosional channel fill, laterally accreting channel fill, and overbank elements. Due to their distinct sedimentological and stratigraphic attributes, each element recognized in this study would have different reservoir characteristics, including vertical and lateral connectivity (Table 1).

Erosional channel-fill elements:

This element exhibits a predominance of medium- to very-coarse sandstone bodies (1.5 to 9 meters thick and 50 to 200 meters wide in a direction perpendicular to the paleocurrent), arranged in amalgamated and poorly stratified sandstones towards the channel axis (FA 1) and less amalgamated sandstones in the channel margins (FA 2). They would result in a volumetrically significant reservoir, where a paucity of interbedded fine-grained layers (NTG > 0.9) result in high vertical and lateral connectivity. Thin-bedded and fine-grained horizons are observed mainly at the lateral extremes of the channel complex, where sandstones of the channel margin pinch-out (FA 2).

Amalgamated sandstone beds often display abundant mud-clast layers or are interstratified with laterally persistent mud-clast breccias (Figs. 13B, 14B). The frequency of these levels indicates that they would not constitute a permeability barrier, although they may create a tortuous network of permeable conduits (Fig. 14B). However, while reservoir continuity is not affected, total reservoir sandstone volume would be reduced because of abundant mudstone clasts (NTG 0.7 – 0.8) and critically may be overrepresented or misinterpreted as shale-facies if particularly abundant in well bores (e.g., Stanbrook and Bentley, 2022).

The presence of c. 2-meters-thick, chaotic deposits (facies 1a and 1b, Unit 2B) at the base of the axial channel fill with a horizontal distribution of a few tens of meters can negatively influence the connectivity of the reservoir or even constitute a permeability barrier (e.g., Schwarz and Arnott, 2007).

These architectural elements stack vertically in units 2B and 2C to form a single “reservoir” at least 6 meters thick and up to 250 meters wide and is entirely interconnected, with erosional surfaces placing underlying sandstones in direct contact with overlying and lateral sandstones (Fig. 6). The same architectural element is recognizable in Unit 1A, but in this case they form small, isolated channel fills at least 200 meters wide and up to 1.5 meters thick, encased in heterolithic strata and are not interconnected.

Laterally accreting elements:

Single lateral accreting elements exhibit a thickness of 1 to 2.5 meters and good lateral continuity (perpendicular to the paleocurrent) ranging from 90 to 450 meters, generating a potential reservoir architecture that is often a few meters thin but with high lateral continuity. Typically, these elements are characterized by laterally stacked sigmoidal bodies, which display distinct characteristics in different positions of the sigmoid, which can enhance or reduce the reservoir quality. Lateral accretion packages show amalgamation downdip, but are commonly separated by laterally extensive, thin-bedded intervals diminishing their vertical connectivity. The toe-set (FA5) is usually composed of coarse and amalgamated sandstones with good connectivity. The middle-set (FA4) consists of amalgamated thick-bedded sandstones, occasionally exhibiting discontinuous horizons of thin beds that form local permeability barriers but do not affect the potentially high lateral and vertical connectivity of these thick sandstones. The top-set (FA3), on the other hand, provides low lateral and vertical connectivity values due to the presence of thin-bedded sandstones and mudstones.

The presence of mud-clast horizons in the amalgamated sandstones belonging to FA 4 and FA 5 (Figs. 11B, 15B), does not represent permeability barriers but may affect the overall quality and volume of the reservoir (e.g., Schwarz and Arnott, 2007). Since the presence of mud-clast-horizon thickness displays values lower than 40% of the studied interval (Figs. 11B, 15B), we can assume that the impact of mud-clast horizons on the reservoir volumes would be negligible.

The laterally accreted architectural elements (FA3, FA4, and FA5) are laterally stacked in Unit 1B, forming a potential reservoir up to 5 meters thick and at least 500 meters wide (Fig. 6). Unit 3 also shows a similar laterally stacked architectural element generating a potential reservoir 3 meters thick and 300 meters wide (Fig. 6).

Overbank elements:

Impermeable layers that may form barriers to fluid migration are present in the complex, represented by horizons, up to 5 m thick, of thin-bedded siltstones or sandstones and mudstones (NTG < 30%). These heterolithic intervals extend laterally from 50 to 300 meters away from the channel fill in units 2B and 2C. They typically pinch out toward the channel axis due to channel erosion. These laterally extensive and often thick barriers would affect reservoir performance and connectivity, but they are unlikely to vertically compartmentalize the reservoir due to subsequent channel erosion.

These low-permeability intervals range in thickness from 2 to 5 meters and in lateral extent from 50 to 300 meters. The three described elements have distinct reservoir characteristics in terms of connectivity and continuity. Considering the lateral and vertical juxtaposition of elements, it is observed that erosional channel-fill and laterally accreting elements have very good reservoir attributes and are interconnected, creating a continuous reservoir. They are the most common elements and represent 60% of the gross channel-complex sandstone (Table 1). By contrast, the basal part of the complex is composed of small channels not connected to each other. Different scales of permeability-barrier-type facies (overbank elements) were identified and represent 40% of the exposed and preserved outcrop of Complex 7 (Table 1).

What can be inferred from the 2D correlation panel (Fig. 6), and considering the three-dimensionality as sketched in Figure 16, is that the channel complex would represent an individual fluid flow cell where only non-areally extensive permeability barriers (40%; Table 1) are present. However, ongoing larger-scale work (covering the entire lateral extent of Complex 7) leads us to believe that extensive thin-bedded elements developed during local channel-complex abandonment and mud-rich debrites constitute kilometer-scale barrier-type facies that would effectively compartmentalize the channel complex.

Kilometer-scale marlstone-rich intervals likely represent effective permeability barriers between channel complexes. These thick (up to 10 meters) laterally persistent marls (facies f8) and siltstone-rich thin beds separate Complex 7 from the underlying and overlying channel-levee complexes. These marlstone-rich intervals would constitute intraformational seals that would prevent connectivity between channel complexes and pressure communication in analogous reservoirs.

CONCLUSIONS

The late Tortonian channel fills described here represent Channel Complex 7 of the Tachrift System, Taza-Guercif Basin, NE Morocco. The studied outcrops represent an exceptionally exposed part of deposition in and adjacent to a long-lived sediment pathway that accumulated 30 m of predominantly sandstone in a deep-marine slope setting. Based on correlations along a NW-SE-oriented continuous 500-meters-wide outcrop transect, perpendicular to the main paleocurrent direction, the studied part of Complex 7 has been divided into five vertically stacked sedimentary units, each consisting of a unique assemblage of facies, with different internal geometries and bounding surfaces. Statistics compiled for key sedimentological variables enabled quantification of vertical and lateral heterogeneity of facies assemblages and trends between the units.

An idealized evolution of the channel complex begins with the development of small, isolated channel fills, followed by eastward laterally accreting packages deposited in a highly sinuous channel. This phase was interrupted by erosion from a relatively linear channel and greater sediment bypass, followed by filling of the erosional channel with amalgamated and non-amalgamated elements and the development of overbank levees. The late stage of the channel complex is represented by an episode of reincision before reestablishment of laterally accreting packages deposited in sinuous channels. Final deactivation of the channel complex was followed by accumulation of a laterally extensive and c. 10-meters-thick marlstone alternating with thin-bedded sandstones and mudstones interpreted to reflect distal overbank deposition associated with another distant channel.

Six distinct facies association were identified and grouped in three categories based on their distinct depositional styles: (i) erosional channel-fill elements, (ii) laterally accreting elements and (iii) overbank elements.

Each of these depositional elements have distinct reservoir attributes (heterogeneity, connectivity, and continuity), with implications for reservoir properties in analogous systems. Laterally accreting elements and erosional channel-fills elements show good reservoir properties (Table 1), being interconnected, and containing 60% of the gross channel-complex sandstone, creating a single fluid-flow cell where only non-areally extensive permeability barriers are present. The latter are represented principally by overbank and chaotic deposits, representing 40% of the studied channel complex.

This study illustrates the detailed stratigraphic complexity, evolution, and reservoir characterization that can be expected in turbidite-dominated slope channel systems. Moreover, it is a potential analogue for similar systems developed on continent-margin basins that until now were characterized primarily by lower-resolution subsurface data.

ACKNOWLEDGMENTS

We thank the ‘Ministero dell’Università e della Ricerca’ of Italy, the Turbidites Research Group (TRG), and the International Association of Sedimentologists (IAS) for financial support to this project. Authors thank Prof. Imad El Kati and Prof. Hassan Tabyaoui for logistical support. The local Authorities of Douar Tachrift and Ras El Ksar are thanked for providing access to outcrops. We thank Jean Amoussou for computing statistics. Also, we wish to thank Hachimi Family for their hospitality. We thank editors Gillian Apps, Dustin E. Sweet, and George Postma and constructive reviews by Stan Stanbrook and Zane Jobe.

REFERENCES

Abreu, V., Sullivan, M., Pirmez, C., and Mohrig, D., 2003, Lateral accretion packages (LAPs): an important reservoir element in deep water sinuous channels: Marine and Petroleum Geology, v. 20, p. 631—648.

Alpak, F.O., Barton, M.D., and Naruk, S.J., 2013, The impact of fine-scale turbidite channel architecture on deep-water reservoir performance:American Association of Petroleum Geologists , Bulletin, v. 97(2), p. 251–284.

Aniekwena, A.U., McVay, D.A., Ahr, W.M., and Watkins, J.S., 2003, Integrated characterization of the thin-bedded 8 reservoir, Green Canyon 18, Gulf of Mexico: SPE Annual Technical Conference and Exhibition?, SPE-84051.

Arnott, R.W.C., 2007, Stratal architecture and origin of lateral accretion deposits (LADs) and conterminuous inner-bank levee deposits in a base-of-slope sinuous channel, lower Isaac Formation (Neoproterozoic), East-Central British Columbia, Canada: Marine and Petroleum Geology, v. 24, p. 515–528.

Arnott, R.W.C., Tilston, M., Fraino, P., Navarro, L., Dumouchel, G., and Miklovich, N., 2021. Laterally accreting sinuous channels and their deposits: The Goldilocks of deep-water slope systems: Journal of Sedimentary Research, v. 91, p. 451–463.

Bell, D., Soutter, E. L., Cumberpatch, Z. A., Ferguson, R. A., Spychala, Y. T., Kane, I. A., and Eggenhuisen, J. T., 2021, Flow-process controls on grain type distribution in an experimental turbidity current deposit: Implications for detrital signal preservation and microplastic distribution in submarine fans: The Depositional Record, v. 7(3), p. 392–415.

Bernini, M., Boccaletti, M., El Mokhtari, J., Gelati, R., Moratti, G., and Papani, G., 1994, Geologic-structural Map of the Taza–Guercif Neogene basin (North–eastern Morocco). Scale 1: 50.000: Società Elaborazioni Cartografiche, Firenze.

Bernini, M., Boccaletti, M., Moratti, G., and Papani, G., 2000, Structural development of the Taza–Guercif Basin as a constraint for the Middle Atlas Shear Zone tectonic evolution: Marine and Petroleum Geology, v. 17, p. 391–408.

Brunt, R.L., Hodgson, D.M., Flint, S.S., Pringle, J.K., Di Celma, C., Prélat, A., and Grecula, M., 2013, Confined to unconfined: Anatomy of a base of slope succession, Karoo Basin, South Africa: Marine and Petroleum Geology, v. 41(1), p. 206–221.

Camacho, H., Busby, C.J., and Kneller, B., 2002, A new depositional model for the classical turbidite locality at San Clemente State Beach, California: American Association of Petroleum Geologists , Bulletin, v. 86 (9), p. 1543–1560.

Campion, K.M., 2005, Architecture and lithofacies of the Capistrano Formation (Miocene-Pliocene), San Clemente, California, Pacific Section SEPM (Society for Sedimentary Geology) Field Trip Guide Book, v. 100, p. 42.

Campion, K.M., Sprague, A.R., Mohrig, D., Lovell, R.W., Drzewiecki, P.A., Sullivan, M.D., Ardill, J.A., Jensen, G.N., and Sickafoose, D.K., 2000, Outcrop expression of confined channel complexes: SEPM (Society for Sedimentary Geology), Deep-Water Reservoirs of the World, Gulf Coast Section, 20th Annual Research Conference (Eds. Weimar, P., Slatt, R.M., Coleman, J., Rosen, N.C., Nelson, H., Bouma, A.H., Styzen, M.J. and Lawrence, D.T.), 127–151.

Capella, W., Barhoun, N., Flecker, R., Hilgen, F.J., Kouwenhoven, T., Matenco, L.C., Sierro, F.J., Tulbure, M.A., Yousfi, M.Z., and Krijgsman, W., 2018, Palaeogeographic evolution of the late Miocene Rifian Corridor (Morocco): Reconstructions from surface and subsurface data: Earth-Science Reviews, v. 180, p. 37–59.

Cronin, B.T., Hurst, A., Celik, H., and Türkmen, I., 2000, Superb exposure of a channel, levee and overbank complex in an ancient deep-water slope environment: Sedimentary Geology, v. 132(3–4), p. 205–216.

Cullis, S., Colombera, L., Patacci, M., and McCaffrey, W.D., 2018, Hierarchical classifications of the sedimentary architecture of deep-marine depositional systems: Earth-Science Reviews, v. 179, p. 38–71.

Cunningham, C.M., and Arnott, R.W.C., 2021, Systematic organization of thin-bedded turbidites in ancient deep-marine levees: Possible evidence of rhythmic pulsing in turbidity currents: Journal of Sedimentary Research, v. 91(11), p. 1257–1274.

de Lamotte, D.F., Leturmy, P., Missenard, Y., Khomsi, S., Ruiz, G., Saddiqi, O., Guillocheau, F., and Michard, A., 2009, Mesozoic and Cenozoic vertical movements in the Atlas system (Algeria, Morocco, Tunisia): An overview: Tectonophysics, v. 475(1), p. 9–28.

de Leeuw, J., Eggenhuisen, J.T., and Cartigny, M.J.B., 2018, Linking submarine channel–levee facies and architecture to flow structure of turbidity currents: insights from flume tank experiments: Sedimentology, v. 65(3), p. 931–951.

Dykstra, M., and Kneller, B., 2009, Lateral accretion in a deep-marine channel complex: Implications for channellized flow processes in turbidity currents: Sedimentology, v. 56(5), p. 1411–1432.

Felletti, F., Marini, M., El Kati, I., and Tabyaoui, H., 2020, The Tachrift channel-levée turbidite complexes (Tortonian) of the Taza-Guercif basin (South Rifian Corridor, NE Morocco): Journal of Maps, v. 16(2), p. 902–917.

Felletti, F., Pantopoulos, G., Zuffetti, C., Reguzzi, S., Invernizzi, D., Bellin, N., Marini, M., El Kati, I., Savi, E., Tabyaoui, H. and McArthur, A., 2023, The Tachrift Project: sedimentary architecture of turbidite channel-levée deposits (Tachrift Turbidite System, Taza-Guercif Basin, Tortonian, NE Morocco): Rendiconti Online Società Geologica Italiana, v. 59, p. 80–88.

Fildani, A., Hubbard, S.M., Covault, J.A., Maier, K.L., Romans, B.W., Traer, M., and Rowland, J.C., 2013, Erosion at inception of deep-sea channels. Marine and Petroleum Geology, v. 41(1), p. 48–61.

Fonnesu, M., and Felletti, F., 2019, Facies and Architecture of a Sand-Rich Turbidite System in an evolving Collisional-Trench Basin: A Case History from the Upper Cretaceous-Paleocene Gottero System (NW Apennines): Rivista italiana di paleontologia e stratigrafia, v. 125(2), p. 449–487.

Gardner, M.H., and Borer, J.M., 2000, Submarine channel architecture along a slope to basin profile, Brushy Canyon Formation, west Texas: in Fine-Grained Turbidite Systems, eds., AAPG Memoir 72: SEPM Special Publication, v. 68, p.195–215.

Gelati, R., Moratti, G., and Papani, G., 2000, The Late Cenozoic sedimentary succession of the Taza-Guercif Basin, South Rifian Corridor, Morocco: Marine and Petroleum Geology, v. 17, p. 373–390.

Godo, T.J., 2006, Identification of stratigraphic traps with subtle seismic amplitude effects in Miocene channel/levee sand systems, NE Gulf of Mexico, in M. R. Allen, G. P. Goffrey, R. K. Morgan, and J. M. Walker, eds., The deliberate search for the stratigraphic trap: Geological Society, of London, Special Publication, v. 254, p. 127–151.

Hafid, M., Zizi, M., Bally, A.W., and Ait Salem, A., 2006, Structural styles of the western onshore and offshore termination of the High Atlas, Morocco: Comptes Rendus - Geoscience, v. 338(1–2), p. 50–64.

Hansen, L.A.S., Callow, R.H.T., Kane, I.A., Gamberi, F., Rovere, M., Cronin, B.T., and Kneller, B.C., 2015, Genesis and character of thin-bedded turbidites associated with submarine channels: Marine and Petroleum Geology, v. 67, p. 852–879.

Hansen, L., Callow, R., Kane, I., and Kneller, B., 2017, Differentiating submarine channel-related thin-bedded turbidite facies: Outcrop examples from the Rosario Formation, Mexico: Sedimentary Geology, v. 358, p. 19–34.

Hubbard, S.M., Romans, B.W., and Graham, S.A., 2008, Deep-water foreland basin deposits of the Cerro Toro Formation, Magallanes basin, Chile: Architectural elements of a sinuous basin axial channel belt: Sedimentology, v. 55(5), p. 1333–1359.

Hubbard, S.M., de Ruig, M.J., and Graham, S.A., 2009, Confined channel-levee complex development in an elongate depo-center: Deep-water Tertiary strata of the Austrian Molasse basin: Marine and Petroleum Geology, v. 26(1), p. 85–112. Hubbard, S.M., Covault, J.A., Fildani, A., and Romans, B.W., 2014, Sediment transfer and deposition in slope channels: Deciphering the record of enigmatic deep-sea processes from outcrop: Geological Society of America Bulletin , v. 126(5–6), p. 857–871.

Hubbard, S.M., Jobe, Z.R., Romans, B.W., Covault, J.A., Sylvester, Z., and Fildani, A., 2020, The stratigraphic evolution of a submarine channel: Linking seafloor dynamics to depositional products: Journal of Sedimentary Research, v. 90(7), p. 673–686.

Jackson, A., Stright, L., Hubbard, S.M., and Romans, B.W., 2019, Static connectivity of stacked deep-water channel elements constrained by high-resolution digital outcrop models: American Association of Petroleum Geologists, Bulletin, v. 103(12), p. 2943–2973.

Janocko, M., Nemec, W., Henriksen, S., and Warchoł, M., 2013, The diversity of deep-water sinuous channel belts and slope valley-fill complexes: Marine and Petroleum Geology, v. 41, p. 7–34.

Jobe, Z.R., Bernhardt, A., and Lowe, D.R., 2010, Facies and architectural asymmetry in a conglomerate-rich submarine channel fill, cerro toro formation, Sierra Del Toro, Magallanes Basin, Chile: Journal of Sedimentary Research, v. 80(12), p. 1085–1108.

Jobe, Z.R., Sylvester, Z., Parker, A.O., Howes, N., Slowey, N., and Pirmez, C., 2015, Rapid adjustment of submarine channel architecture to changes in sediment supply: Journal of Sedimentary Research, v. 85(6), p. 729–753.

Kane, I.A., and Clare, M.A., 2019, Dispersion, accumulation, and the ultimate fate of microplastics in deep-marine environments: A review and future directions: Frontiers in Earth Science, v. 7, p. 1–27.

Kane, I.A., Kneller, B.C., Dykstra, M., Kassem, A., and McCaffrey, W.D., 2007, Anatomy of a submarine channel-levee: An example from Upper Cretaceous slope sediments, Rosario Formation, Baja California, Mexico: Marine and Petroleum Geology, v. 24(6–9), p. 540–563.

Kneller, B., 2003, The influence of flow parameters on turbidite slope channel architecture: Marine and Petroleum Geology, v. 20(6–8), p. 901–910.

Kneller, B., Bozetti, G., Callow, R., Dykstra, M., Hansen, L., Kane, I., Li, P., McArthur, A., Catharina, A.S., Dos Santos, T., and Thompson, P., 2020, Architecture, process, and environmental diversity in a late cretaceous slope channel system: Journal of Sedimentary Research, v. 90(1), p. 1–26.

Kominz, M.A., Patterson, K., and Odette, D., 2011, Lithology dependence of porosity in slope and deep marine sediments: Journal of Sedimentary Research, v. 81(10), p. 730–742.

Krijgsman, W., and Langereis, C.G., 2000, Magnetostratigraphy of the Zobzit and Koudiat Zarga sections (Taza-Guercif basin, Morocco): implications for the evolution of the Rifian Corridor: Marine and Petroleum Geology, v. 17(3), p. 359–371.

Krijgsman, W., Langereis, C.G., Zachariasse, W.J., Boccaletti, M., Moratti, G., Gelati, R., Iaccarino, S., Papani, G., and Villa, G., 1999, Late Neogene evolution of the Taza–Guercif Basin (Rifian Corridor, Morocco) and implications for the Messinian salinity crisis: Marine Geology, v. 153, p. 147–160.

Kus, K.B., Jobe, Z.R., Laugier, F., Walker, W., and Sullivan, M., 2022, Quantifying the lateral heterogeneity of distal submarine lobe deposits, Point Loma Formation, California: Implications for subsurface lateral facies prediction: The Depositional Record, v. 8(2), p. 472–501.

La Marca, K., Bedle, H., Stright, L., and Marfurt, K., 2023, Sensitivity analysis of seismic attributes parametrization to reduce misinterpretations: Applications to deepwater channel complexes, Marine and Petroleum Geology, v. 153, art. no. 106309.

Lewis, M.M., Mugwanya, K.E., and Mayall, M., 2023, Quantitative analysis of the structural evolution of salt diapirs and their impact on sediment routing and the architecture of deep-water channel reservoirs, Venus field offshore Angola: Marine and Petroleum Geology, v. 155, art. no. 106380.

Li, P., Kneller, B.C., Hansen, L., and Kane, I.A., 2016, The classical turbidite outcrop at San Clemente, California revisited: An example of sandy submarine channels with asymmetric facies architecture: Sedimentary Geology, v. 346, p. 1–16.

Li, P., Kneller, B., Thompson, P., Bozetti, G., and dos Santos, T., 2018, Architectural and facies organisation of slope channel fills: Upper Cretaceous Rosario Formation, Baja California, Mexico: Marine and Petroleum Geology, v. 92, p. 632–649.

Liu, L., Zhang, T., Zhao, X., Wu, S., Hu, J., Wang, X., and Zhang, Y., 2013, Sedimentary architecture models of deepwater turbidite channel systems in the Niger Delta continental slope, West Africa: Petroleum Science, v. 10, p. 139–148.

Lowe, D.R., 1982, Sediment gravity flows; II, Depositional models with special reference to the deposits of high-density turbidity currents: Journal of Sedimentary Petrology, v. 52(1), p. 279–297.

Macauley, R.V, and Hubbard, S.M., 2013, Slope channel sedimentary processes and stratigraphic stacking, Cretaceous Tres Pasos Formation slope system, Chilean Patagonia: Marine and Petroleum Geology, v. 41, p. 146–162.

Macdonald, H.A., Peakall, J., Wignall, P.B., and Best, J., 2011, Sedimentation in deep-sea lobe-elements: implications for the origin of thickening-upward sequences: Geological Society of London, Journal , v. 168, p. 319–332.

Maier, K.L., Fildani, A., McHargue, T.R., Paull, C.K., Graham, S.A., and Caress, D.W., 2012, Punctuated deep-water channel migration: High-resolution subsurface data from the lucia chica channel system, offshore California, U.S.A.: Journal of Sedimentary Research, v. 82(1–2), p. 1–8.

Marini, M., Pantopoulos, G., Invernizzi, D., Felletti, F., El Kati, I., and McArthur, A., 2025, Temporal and spatial changes in style of accretion at the bend of a sinuous turbidite slope channel (Channel Levee Complex 5, Tachrift System of NE Morocco): Journal of Sedimentary Research, v. 95, in press.

Marshall, J.D., Tucker, O.D., and Lovelock, C.E., 2016, Goldeneye: modelling a depleted field for carbon capture–how much uncertainty is left?: Petroleum Geoscience, v. 22(1), p. 37–45.

McArthur, A.D., Tek, D.E., Poyatos-Moré, M., Colombera, L., and McCaffrey, W.D., 2024, Deep-ocean channel-wall collapse order of magnitude larger than any other documented: Communications Earth & Environment, v. 5(1), p. 143.

McHargue, T., Pyrcz, M.J., Sullivan, M.D., Clark, J.D., Fildani, A., Romans, B.W., Covault, J.A., Levy, M., Posamentier, H.W., and Drinkwater, N.J., 2011, Architecture of turbidite channel systems on the continental slope: Patterns and predictions: Marine and Petroleum Geology, v. 28(3), p. 728–743.

Morris, E., 2014, Stratigraphic record of sedimentary processes in submarine channel-levee systems, PhD thesis, University of Liverpool, 465 p.

Mulder, T., and Alexander, J., 2001, The physical character of subaqueous sedimentary density flow and their deposits: Sedimentology, v. 48(2), p. 269–299.

Mutti, E., 1992, Turbidite Sandstones: AGIP, Istituto di geologia, Università di Parma, 275 p.

Mutti, E., and Normark, W. R., 1987, Comparing examples of modern and ancient turbidite systems: problems and concepts, in Leggett, J.K., and Zuffa, G.G., eds., Marine Clastic Sedimentology: Concepts and Case Studies: London, Graham and Trotman, p. 1-38.

Normark, W.R., Posamentier, H., and Mutti, E., 1993, Turbidite systems: state of the art and future directions: Reviews of Geophysics, v. 31(2), p. 91–116.

Patacci, M., 2016, A high-precision Jacob's staff with improved spatial accuracy and laser sighting capability: Sedimentary Geology, v. 335, p. 66–69.

Pettingill, H.S., and Weimer, P., 2002, World-wide deep water exploration and production: Past, present and future: Leading Edge, v. 21, p. 371–376.

Pickering, K.T., and Cantalejo, B., 2015, Deep-marine environments of the middle Eocene upper Hecho Group, Spanish Pyrenees: Introduction: Earth-Science Reviews, v. 144, p. 1–9.

Piper, D.J.W., Hiscott, R.N., and Normark, W.R., 1999, Outcrop-scale acoustic facies analysis and latest Quaternary development of Hueneme and Dume submarine fans, offshore California: Sedimentology, v. 46(1), p. 47–78.

Pirmez, C., and Imran, J., 2003, Reconstruction of turbidity currents in Amazon Channel: Marine and Petroleum Geology, v. 20(6–8), p. 823–849.

Pizzi, M., Whittaker, A.C., Mayall, M., and Lonergan, L., 2023, Structural controls on the pathways and sedimentary architecture of submarine channels: New constraints from the Niger Delta: Basin Research, v. 35(1), p.141–171.

Pohl, F., Eggenhuisen, J.T., Kane, I.A., and Clare, M.A., 2020, Transport and Burial of Microplastics in Deep-Marine Sediments by Turbidity Currents: Environmental Science and Technology, v. 54(7), p. 4180–4189.

Posamentier, H.W., and Kolla, V., 2003, Seismic geomorphology and stratigraphy of depositional elements in deep-water settings: Journal of Sedimentary Research, v. 73(3), p. 367–388.

Pratt, J.R., Barbeau, D.L., Izykowski, T.M., Garver, J.I., and Emran, A., 2016, Sedimentary provenance of the Taza-Guercif Basin, South Rifean Corridor, Morocco: Implications for basin emergence: Geosphere, v. 12(1), p. 221–236.

Reguzzi, S., Marini, M., Felletti, F., El Kati, I., Zuffetti, C., and Tabyaoui, H., 2023, Stratigraphic evolution of a spectacularly exposed turbidite channel belt from the Tachrift System (late Tortonian, north-east Morocco): Sedimentology, v. 70(4), p. 1075–1109.

Reimchen, A.P., Hubbard, S.M., Stright, L., and Romans, B.W., 2016, Using sea-floor morphometrics to constrain stratigraphic models of sinuous submarine channel systems: Marine and Petroleum Geology, v. 77, p. 92–115.

Romans, B.W., Hubbard, S.M., and Graham, S.A., 2009, Stratigraphic evolution of an outcropping continental slope system, Tres Pasos Formation at Cerro Divisadero, Chile: Sedimentology, v. 56(3), p. 737–764.

Sani, F., Zizi, M., and Bally, A.W., 2000, The Neogene–Quaternary evolution of the Guercif Basin (Morocco) reconstructed from seismic line interpretation: Marine and Petroleum Geology, v. 17, p. 343–357.

Schwarz, E., and Arnott, R.W.C., 2007, Anatomy and evolution of a slope channel-complex set (Neoproterozoic Isaac Formation, Windermere Supergroup, southern Canadian Cordillera): implications for reservoir characterization: Journal of Sedimentary Research, v. 77, p. 89–109.

Shao, D., Fan, G., Ma, H., Wang, H., Ding, L., Zuo, G., Lu, Y., and Xu, X., 2024, The complex interaction between channel–levee systems and mass transport complexes in the Pliocene–Quaternary Rakhine Basin, offshore Myanmar: Frontiers in Earth Science, v. 12, art. no. 1286229.

Sprague, A.R.G., Sullivan, M.D., Campion, K.M., Jensen, G.N., Goulding, F.J., Garfield, T.R., Sickafoose, D.K., Rossen, C., Jennette, D.C., Beaubouef, R.T., Abreu, V., Ardill, J., Porter, M.L., and Zelt, F.B., 2002, The physical stratigraphy of deep-water strata: a hierarchical approach to the analysis of genetically related stratigraphic elements for improved reservoir prediction: American Association of Petroleum Geologists, Bulletin, (Abstract), American Association of Petroleum Geologists, Annual Meeting, v. 87, p.10.

Sprague, A.R.G., Garfield, T.R., Goulding, F.J., Beaubouef, R.T., Sullivan, M.D., Rossen, C., Campion, K.M., Sickafoose, D.K., Abreu, V., Schellpeper, M.E., Jensen, G.N., Jennette, D.C., Pirmez, C., Dixon, B.T., Ying, D., Ardill, J., Mohrig, D.C., Porter, M.L., Farrell, M.E., and Mellere, D., 2005, Integrated slope channel depositional models: the key to successful prediction of reservoir presence and quality in offshore west Africa: Veracruz, Mexico, Colegio de Ingenenieros Petroleros de Mexico, Cuarto EExitep, p. 1–13.

Stanbrook, D.S., and Bentley, M., 2022, Practical turbidite interpretation: The role of relative confinement in understanding reservoir architectures: Marine and Petroleum Geology, v. 135.

Talling, P.J., Masson, D.G., Sumner, E.J., and Malgesini, G., 2012, Subaqueous sediment density flows: Depositional processes and deposit types: Sedimentology, v. 59(7), p. 1937–2003.

Talling, P.J., Allin, J., Armitage, D.A., Arnott, R.W.C., Cartigny, M.J.B., Clare, M.A., Felletti, F., Covault, J.A., Girardclos, S., Hansen, E., Hill, P.R., Hiscott, R.N., Hogg, A.J., Clarke, J.H., Jobe, Z.R., Malgesini, G., Mozzato, A., Naruse, H., Parkinson, S., Peel, F.J., Piper, D.J.W., Pope, E., Postma, G., Rowley, P., Sguazzini, A., Stevenson, C.J., Sumner, E.J., Sylvester, Z., Watts, C., and Xu, J., 2015, Key future directions for research on turbidity currents and their deposits: Journal of Sedimentary Research, v. 85(2), p. 153–169.

Tek, D.E., Poyatos-Moré, M., Patacci, M., McArthur, A.D., Colombera, L., Cullen, T.M., and McCaffrey, W.D., 2020, Syndepositional tectonics and mass-transport deposits control channelized, bathymetrically complex deep-water systems (Aínsa depocenter, Spain): Journal of Sedimentary Research, v. 90(7), p. 729–762.

Tek, D.E., McArthur, A.D., Poyatos-Moré, M., Colombera, L., Patacci, M., Craven, B., and McCaffrey, W.D., 2021, Relating seafloor geomorphology to subsurface architecture: How mass-transport deposits and knickpoint-zones build the stratigraphy of the deep-water Hikurangi Channel: Sedimentology, v. 68(7), p. 3141–3190.Valle-Falcones, L.M., Grima-Olmedo, C., Rodríguez-Pons Esparver, R., and Zamarro-Toves, E., 2023, Evaluation and Economics of Shale Gas Reserves in the Flysch-Eocene Formation of the Jaca Basin: Applied Sciences, v. 13(3), p. 1732.

Vendettuoli, D., Clare, M.A., Hughes Clarke, J.E., Vellinga, A., Hizzet, J., Hage, S., Cartigny, M.J.B., Talling, P.J., Waltham, D., Hubbard, S.M., Stacey, C., and Lintern, D.G., 2019, Daily bathymetric surveys document how stratigraphy is built and its extreme incompleteness in submarine channels: Earth and Planetary Science Letters, v. 515, p. 231–247.

Weimer, P., and Pettingill, H.S., 2007, Deep-water exploration and production: A global overview: Atlas of deep-water outcrops of the world: American Association of Petroleum Geologists, Studies in Geology v. 56, p. 29.

Weimer, P., Slatt, R.M., Dromgoole, P., Bowman, M., and Leonard, A., 2000, Developing and managing turbidite reservoirs - case histories and experiences: results of the 1998 European Association of Geoscientists and Engineers / American Association of Petroleum Geologists, research conference: American Association of Petroleum Geologists, Bulletin, v. 84, p. 453-465.

Wynn, R.B., Cronin, B.T., and Peakall, J., 2007, Sinuous deep-water channels: Genesis, geometry and architecture: Marine and Petroleum Geology, v. 24(6–9), p. 341–387.

Zhang, W.B., Duan, T.Z., Liu, Z.Q., Liu, Y.F., Zhao, L., and Xu, R., 2017, Architecture mode, sedimentary evolution and controlling factors of deepwater turbidity channels: A case study of the M Oilfield in West Africa: Petroleum Science, v. 14(3), p. 493–506.

Zuffetti, C., Felletti, F., and Marini, M., 2023, Turbidite channel-levée transitions: insights from the Tachrift system (Complex 6, Taza–Guercif Basin, NE Morocco): Società Geologica Italiana Rendiconti Online, v. 59, p. 21–27.

FIGURES

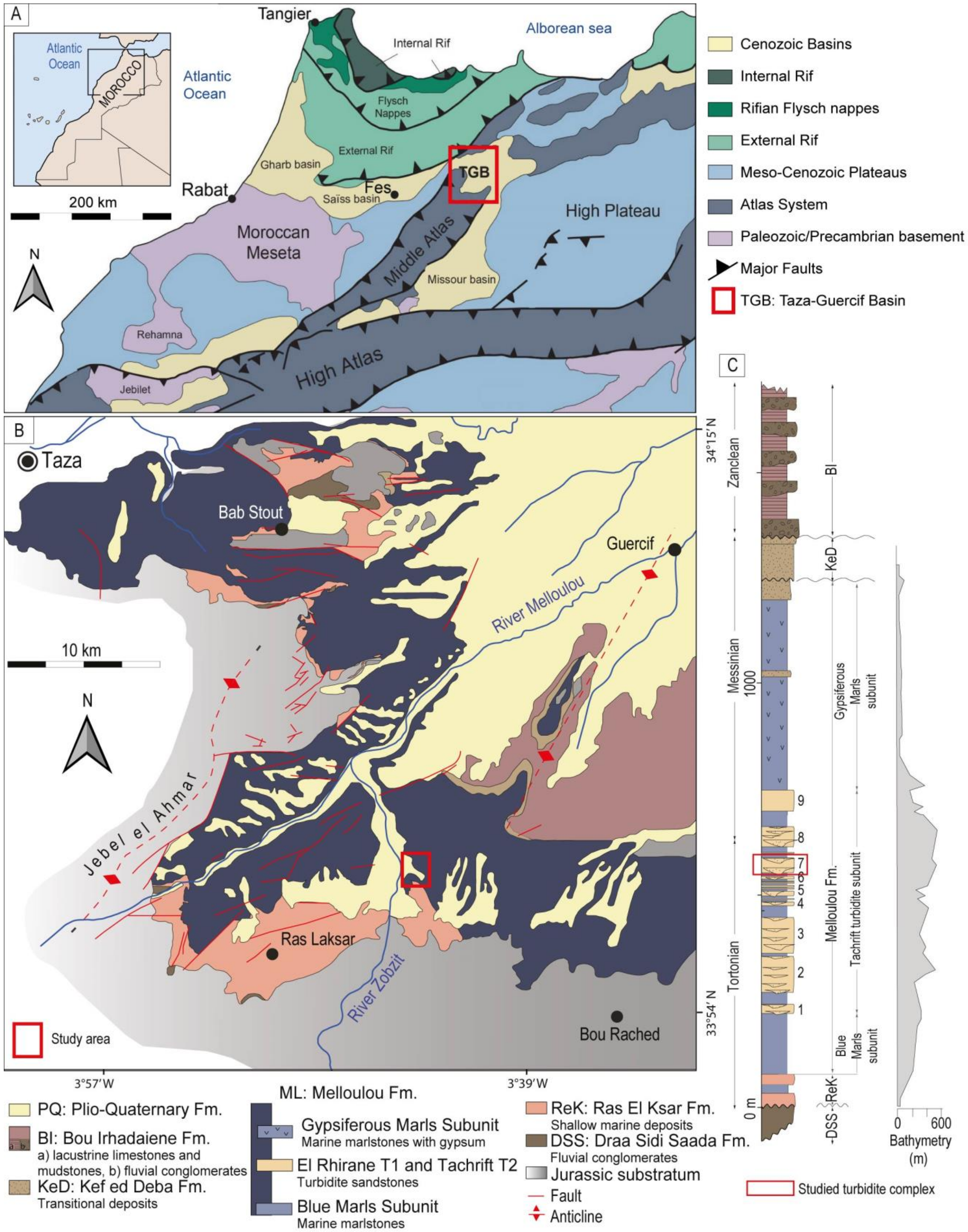

Fig. 1: A) Geological map of northern Morocco illustrating key structural elements, main terrains, and Cenozoic basins, with inset showing location in Morocco (modified after Hafid et al., 2006). B) Geological map of the Taza-Guercif Basin (TGB) with study area in red box

(modified, after Bernini et al., 1994). C) Stratigraphy of the Zobzit section with paleobathymetry and the nine channel-levee complexes of Felletti et al. (2020) (modified after Krijgsman et al., 1999).

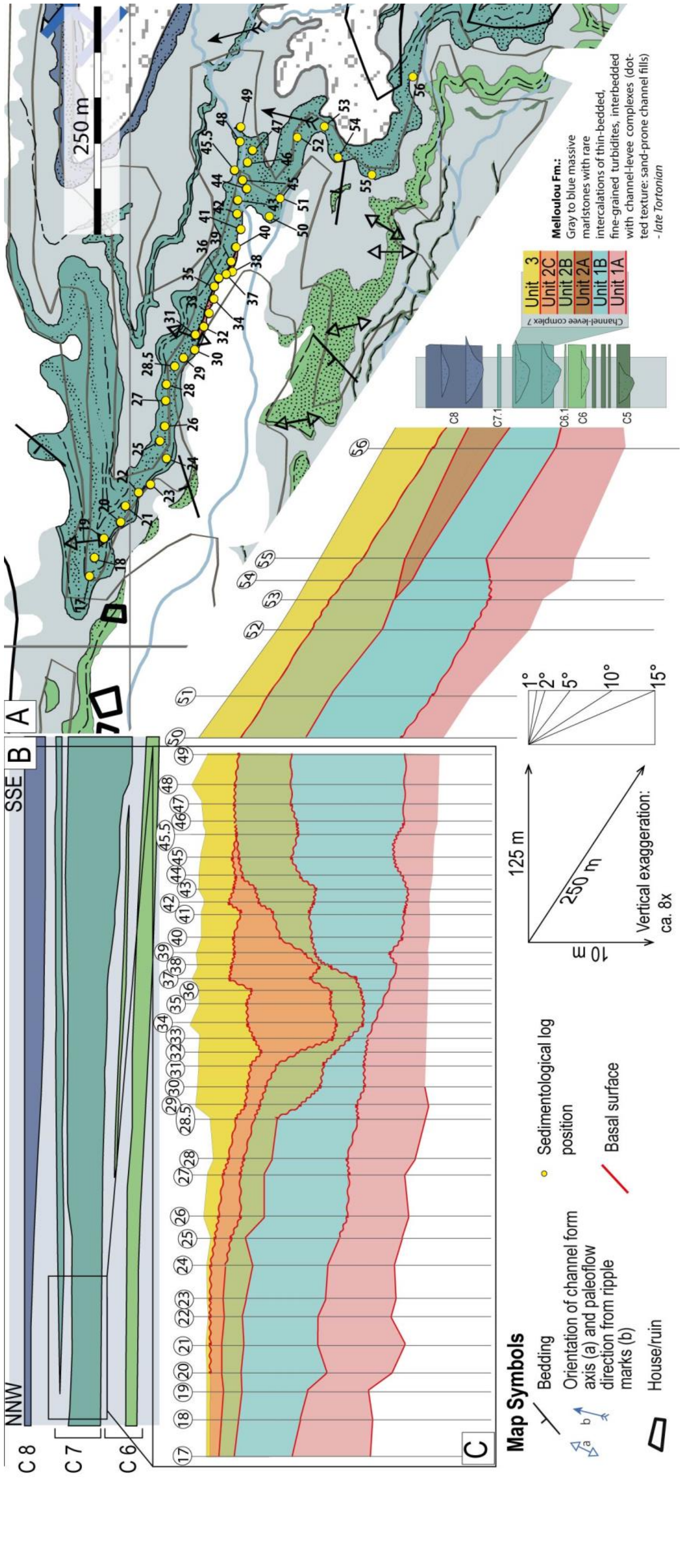

A
B
C
250 m
NNW
SSE
C 8
C 7
C 6
Channel-levee complex 7
C8
C7.1
C6.1
C6
C5
Unit 3
Unit 2C
Unit 2B
Unit 2A
Unit 1B
Unit 1A
Mellouolou Fm.:
Gray to blue massive marlstones with rare intercalations of thin-bedded, fine-grained turbidites, interbedded with channel-levee complexes (dotted texture: sand-prone channel fills) - late Tortonian
Map Symbols
Bedding
Orientation of channel form axis (a) and paleoflow direction from ripple marks (b)
House/ruin
Sedimentological log position
Basal surface
125 m
250 m
10 m
Vertical exaggeration: ca. 8x
1°
2°
5°
10°
15°

Fig. 2: A) Geological map showing the Complex 7 outcrop and location of sedimentary logs (modified after Felletti et al., 2020). B) Stratigraphic cross section showing the stratigraphic relationship between complexes 6, 7, and 8. C) Correlation panels for Complex 7; this work focuses on the NE outcrop in between the log 17 and log 49.

Facies	Code	Name	Thickness [cm]	Grain size	Sedimentary features	Process
	f1a	Sand-dominated chaotic	50-100	/	Plastically deformed sandy beds, granules to cobbles polygenic extra clasts, bioturbation and shell fragments.	Deposition due to a cohesive, plastic, laminar sand-dominated debris flow. *(Lowe, 1982)*
	f1b	Mud-dominated chaotic	150-300	/	Mud clasts, polygenic granules to pebbles clasts and biogenic fragments. Decimetric sandstone boulders.	Deposition due to a cohesive, plastic, laminar mud-dominated debris flow. *(Lowe, 1982)*
	f1c	Debrites	10-50	/	Ungraded, extremely bioturbated and oxidated. Wood, coal fragments, and extraclasts.	Deposited due to *en masse* freezing of a cohesive flow. During deposition the grains of different sizes were not segregated by differential setting. *(Talling et al., 2012)*
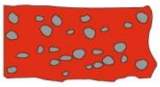	f2	Poorly sorted conglomerate	1-100	cS-Cobbles	Poorly sorted, clast-supported granule to pebble-grained conglomerate. Polygenic clasts. The contacts are tangential and rarely linear. Well-rounded with high-sphericity clasts. Fossil fragments.	The deposition is attributed to traction-carpet sedimentation from a largely bypassing high-density turbidity current. *(Mutti and Normark, 1987)*
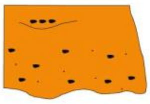	f3	Very thick-bedded massive amalgamated sandstones	S:100-300 M:0	mcS-cS	Massive sandstones. Coarse-grained lenses. Normal grading. Traction carpets. Reworked corals and shell fragments. Mud clast breccias near their erosional bases.	Rapid deposition from an unsteady but fully turbulent sand-rich high-density turbidity current. *(Lowe, 1982; Talling et al., 2012)*
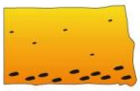	f4	Thick-to medium-bedded amalgamated sandstones	S:50-150 M:0-20	mS-cS	Medium-to coarse-grained sandstones, typically amalgamated. Mud-clast breccias are observed near erosional bases. Bioclastic fragments. At the top, planar-parallel laminations.	Loss of capacity, along with a lack of flow steadiness, of a medium-density turbidity current allowed deposition of this facies. *(Lowe, 1982; Mulder and Alexander, 2001)*
	f5	Medium-bedded structured sandstones	S:15-50 M:0-20	fS-mcS	Plane-parallel and low-angle laminations. Flute and groove marks. Pervasive bioturbation, oxidation, and bioclastic fragments .	Deposition related to a waning, low-to-high- density turbidity currents. *(Lowe, 1982; Li et al., 2016)*
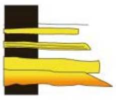	f6	Thin-bedded laminated sand-mud couplets	S:5-20 M:1-5	vfS-mfS	Plane-parallel lamination. Bioturbated mud caps. Ripples are rarely observed at the top of beds.	Deposition from low-density waning flow. *(Lowe, 1982)*
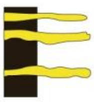	f7	Very thin-bedded sand-mud couplets	S:2-10 M:2-10	vfS-fS	Plane-parallel laminations are rarely observed. Bioturbation and oxidation.	The deposition is attributed to slow deposition from low-density turbidity currents. *(Lowe, 1982; Mulder and Alexander, 2001)*
	f8	Marlstone	S:0 M:1-1000	Mud	Gray in color. Massive. Fossils fragments. Bioturbated.	This facies is interpreted as hemipelagic background sedimentation and also from deposition from the least concentrated part of a low-density turbidity current. *(Mutti, 1992)*

Not to scale

Fig. 3: Summary of sedimentary facies recognized in channel-levee Complex 7. S: sandstone; M: Mudstone

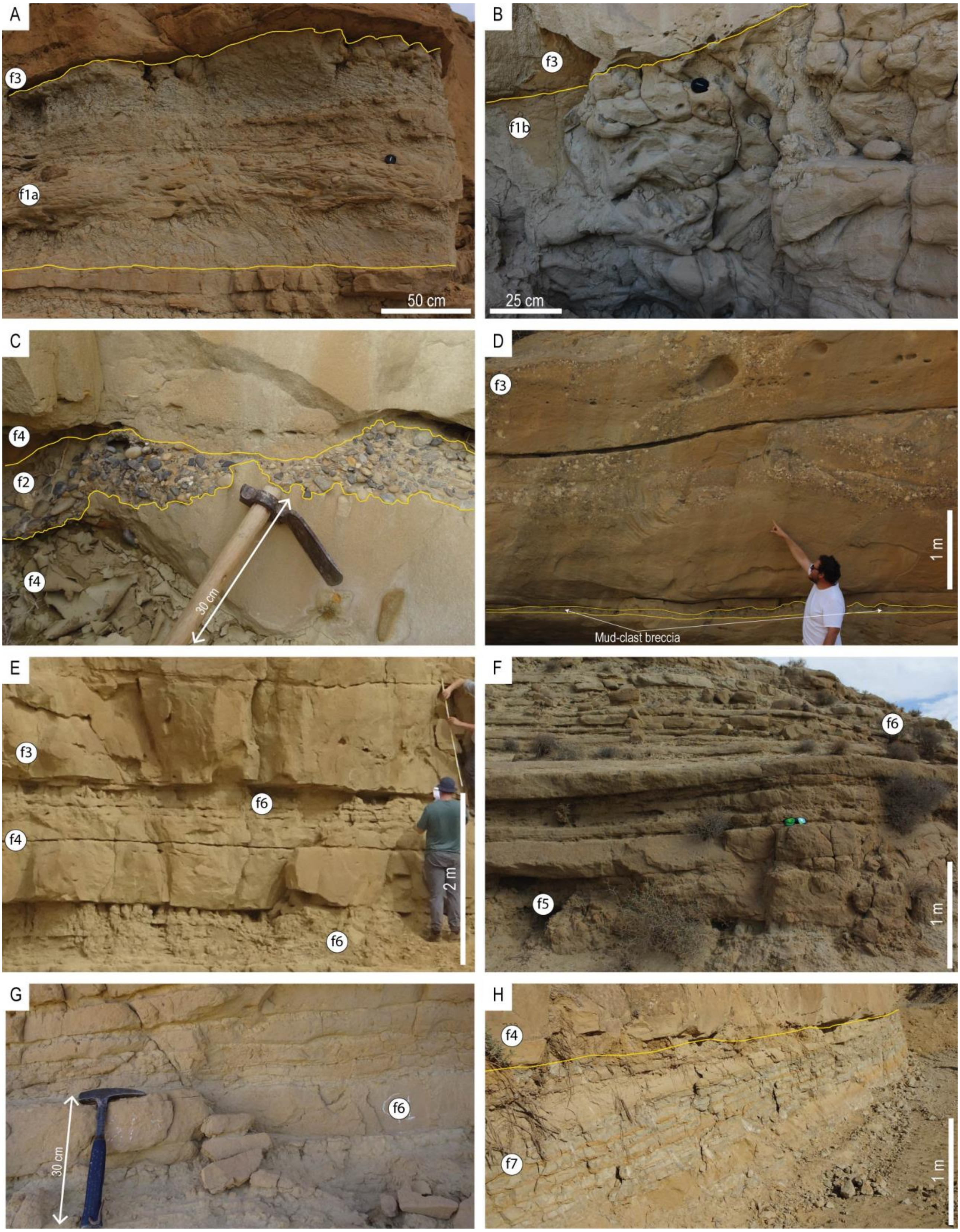

Fig. 4: A) Chaotic facies 1a with deformed sandstone rafts, bioturbation, and oxidation crusts. B) Chaotic facies 1b structureless. C) Conglomerate of facies f2, polygenic grains ranging in size from granules to pebbles. D) Sand beds of facies f3, structureless; the base

of this layer is erosional, and a mud-clast breccia is observed. E) Facies f4, characterized by an alternation of sand beds with variable thickness ranging from 40 cm to a maximum of 150 cm and thin mud-caps (maximum thickness around 20 cm). F) Facies f5, showing sandstone bed with thickness ranging from 15 to 50 cm and thin mud-caps. G) Sandstone beds in facies f6 (thickness ranging from 5 to 20 cm) separated by mud-cap (1-5 cm). H) Facies f7, characterized by an alternation of sand and mud with comparable thicknesses (from a few cm to a maximum of 10 cm).

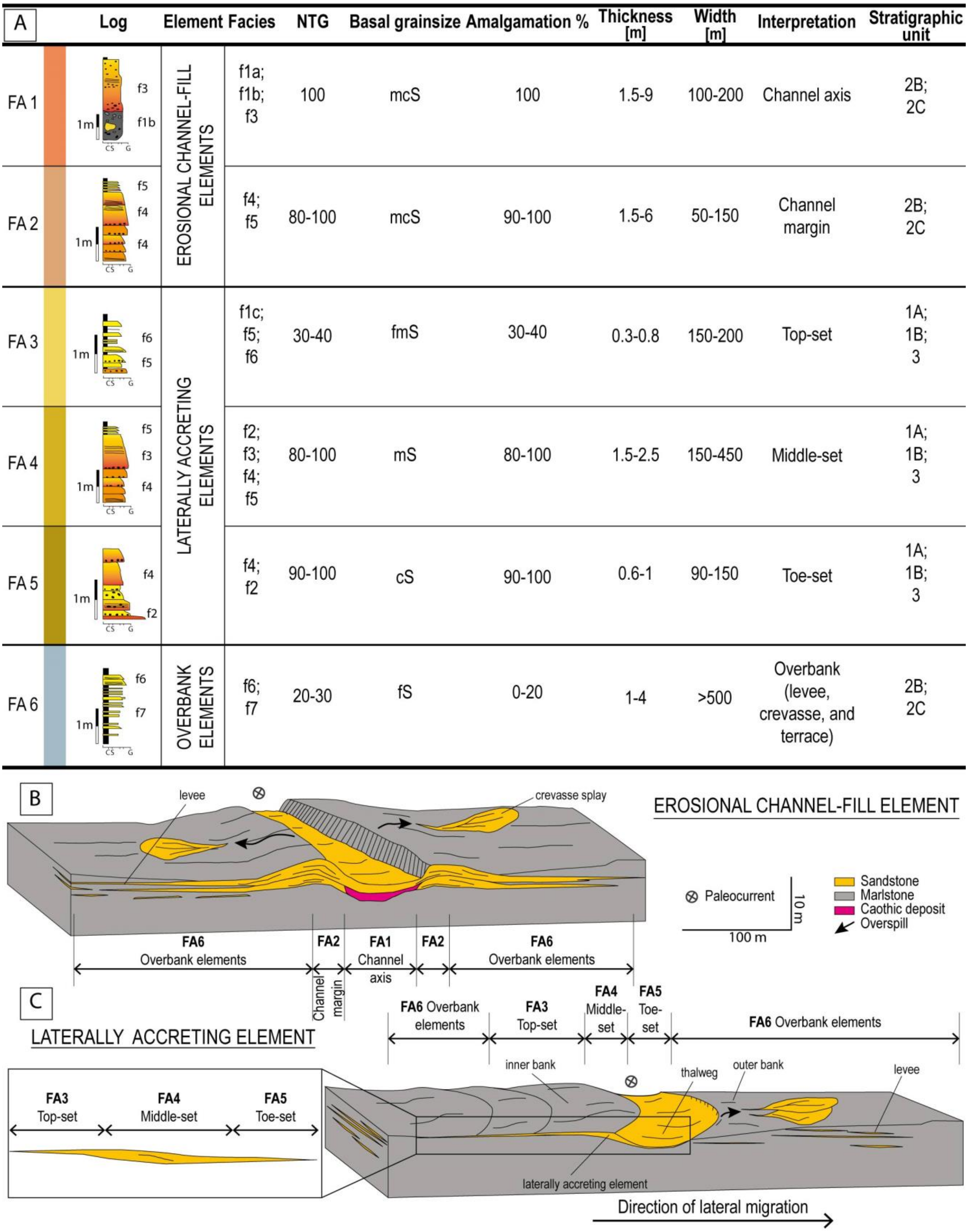

A	Log	Element	Facies	NTG	Basal grainsize	Amalgamation %	Thickness [m]	Width [m]	Interpretation	Stratigraphic unit
FA 1	f3, f1b (1m; cS G)	EROSIONAL CHANNEL-FILL ELEMENTS	f1a; f1b; f3	100	mcS	100	1.5-9	100-200	Channel axis	2B; 2C
FA 2	f5, f4, f4 (1m; cS G)	EROSIONAL CHANNEL-FILL ELEMENTS	f4; f5	80-100	mcS	90-100	1.5-6	50-150	Channel margin	2B; 2C
FA 3	f6, f5 (1m; cS G)	LATERALLY ACCRETING ELEMENTS	f1c; f5; f6	30-40	fmS	30-40	0.3-0.8	150-200	Top-set	1A; 1B; 3
FA 4	f5, f3, f4 (1m; cS G)	LATERALLY ACCRETING ELEMENTS	f2; f3; f4; f5	80-100	mS	80-100	1.5-2.5	150-450	Middle-set	1A; 1B; 3
FA 5	f4, f2 (1m; cS G)	LATERALLY ACCRETING ELEMENTS	f4; f2	90-100	cS	90-100	0.6-1	90-150	Toe-set	1A; 1B; 3
FA 6	f6, f7 (1m; cS G)	OVERBANK ELEMENTS	f6; f7	20-30	fS	0-20	1-4	>500	Overbank (levee, crevasse, and terrace)	2B; 2C

Fig. 5: A) Main features of the six facies association recognized in this work. B) Erosional channel-fill element depositional style. C) Laterally accreting element depositional style.

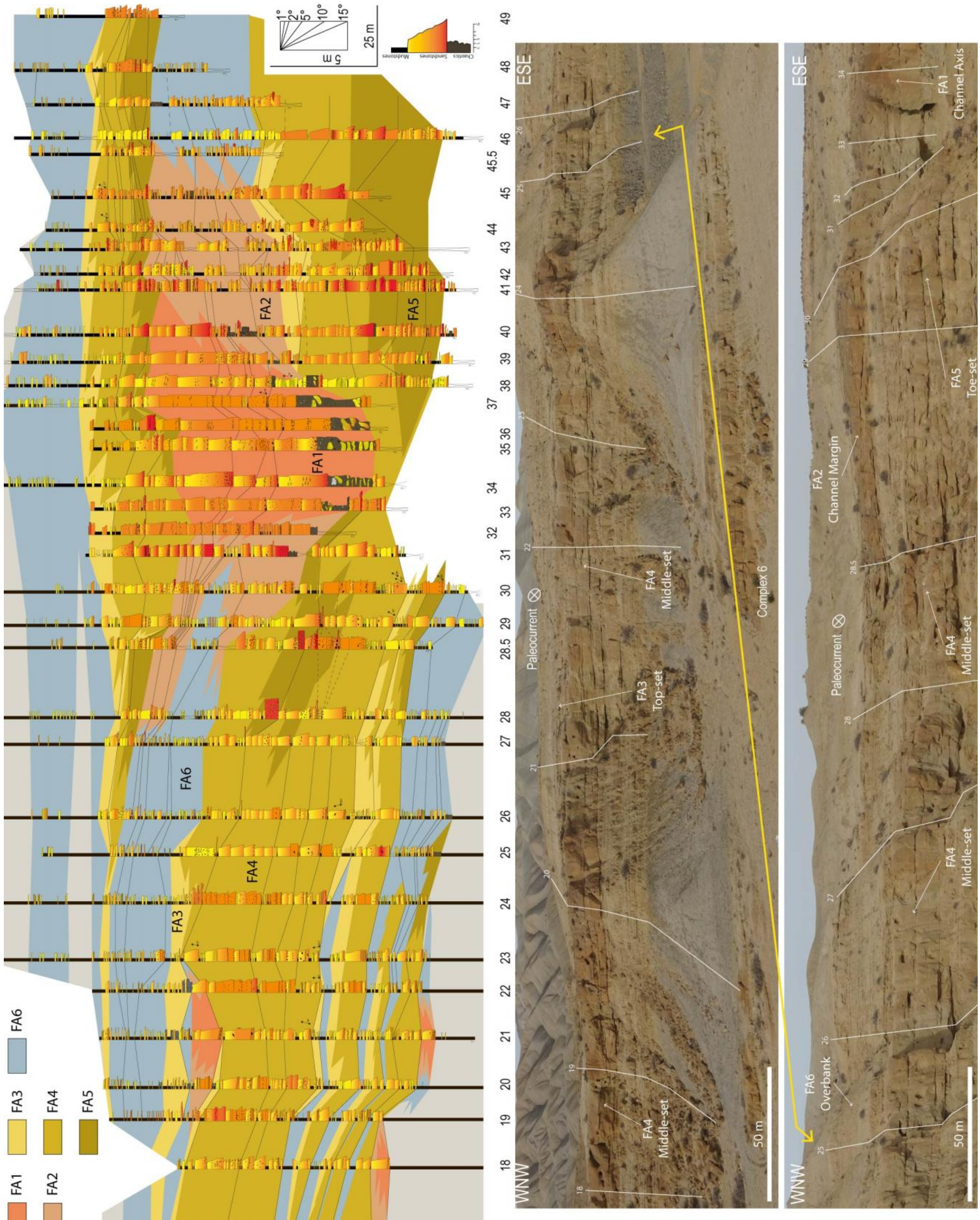

Fig. 6: Correlational panel showing the subdivision in facies association of the outcrop. The two panoramic pictures below show the distribution of the facies association in outcrop view.

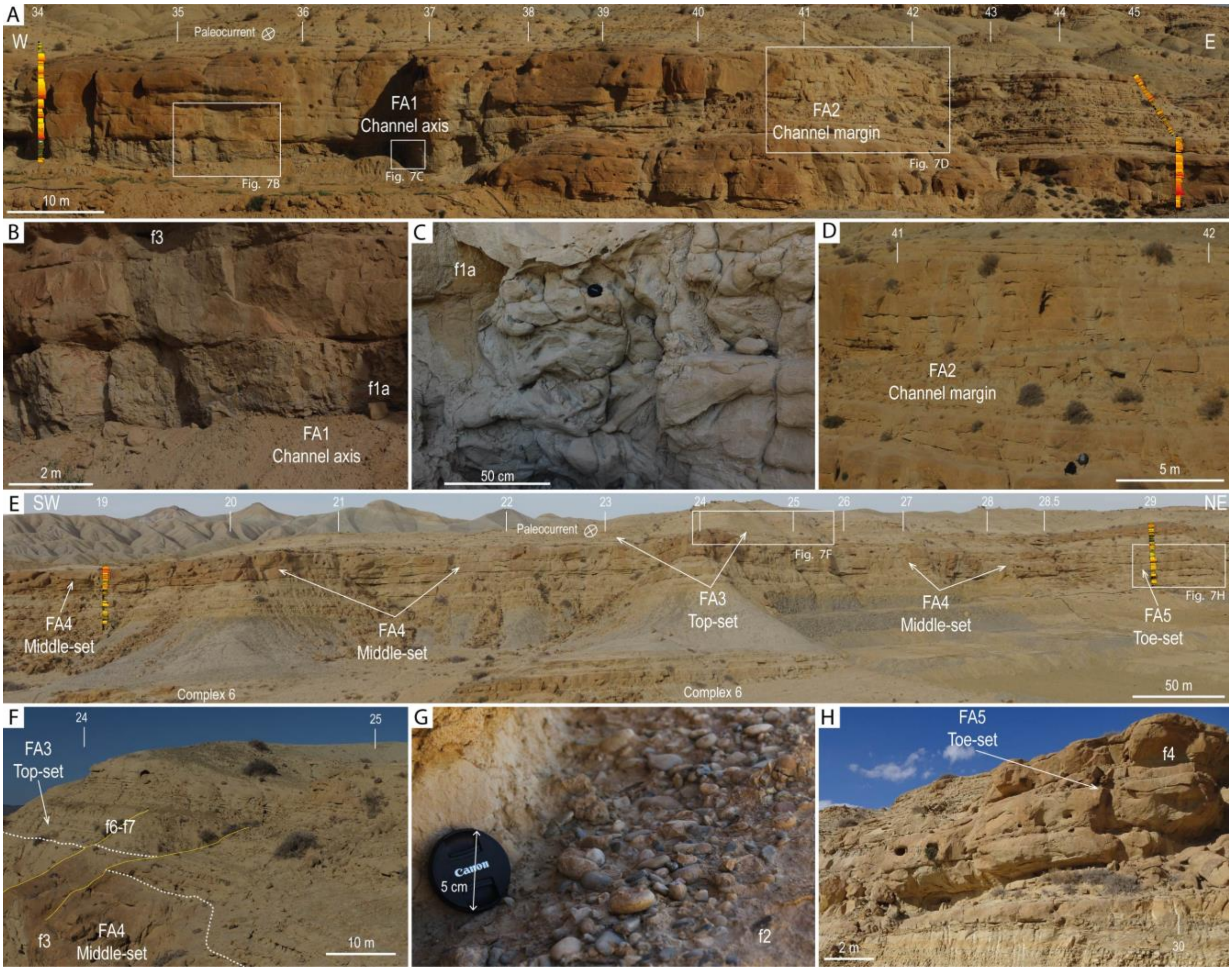

Fig. 7: A) Panoramic view of the erosional channel-fill element, with thick sand beds and chaotic deposits of FA1 (Channel axis) and less amalgamated beds of FA2 (Channel margin). B) Detail of the two facies (f1a and f3) composing FA1. C) Chaotic deposits (facies f1a) belonging to FA1. D) Characteristic less amalgamated beds (facies f4 and f5) of FA2. E) Panoramic view of the laterally accreting element. F) FA3 characterized by thin beds (facies f6-f7). G) Facies f2 at the base of FA5. H) Amalgamated beds with erosional bases of facies f4, characteristic of FA5.

1240 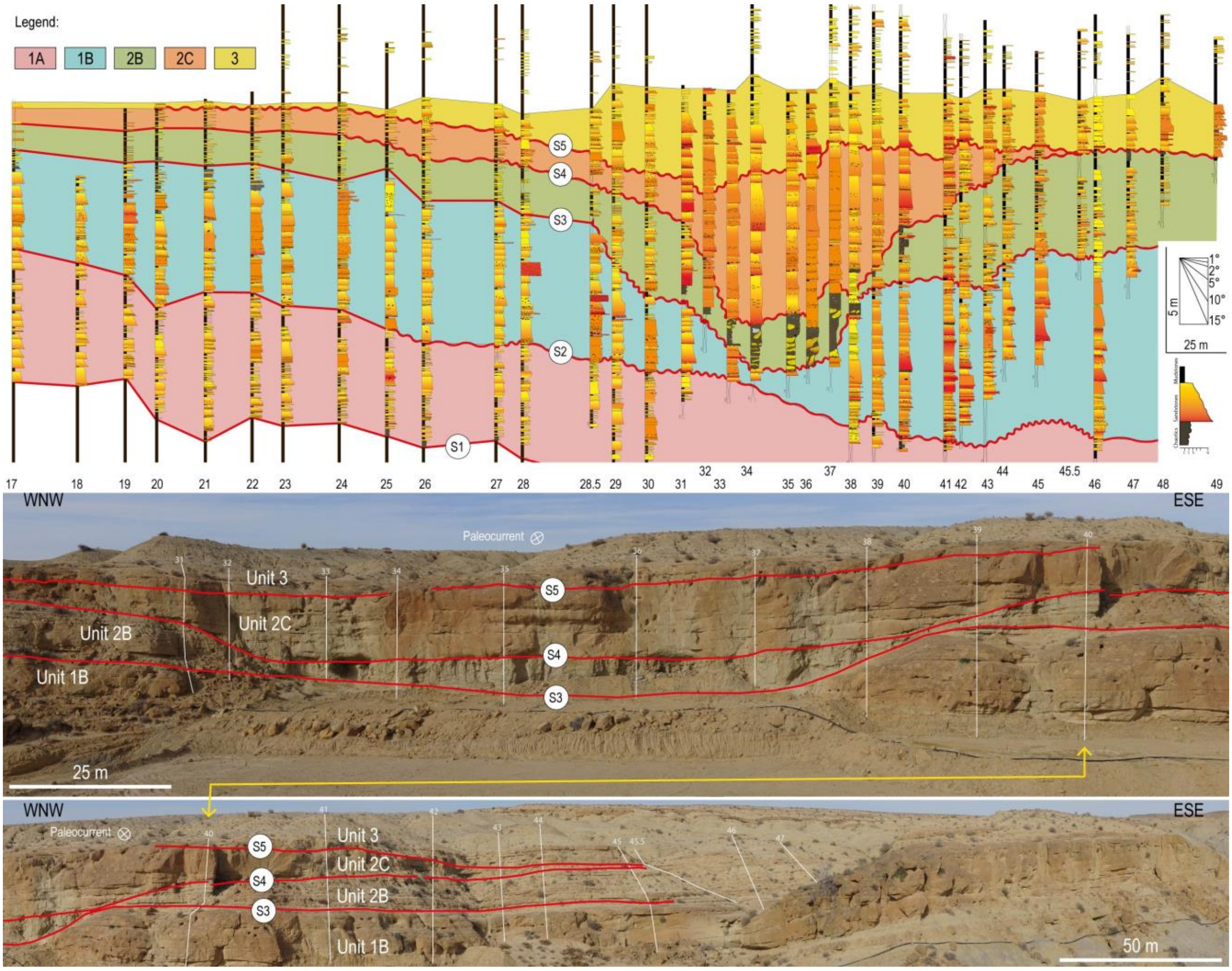

1241 **Fig. 8:** Correlational panel showing the subdivision in units. The two panoramic pictures

1242 show the units in outcrop view. S1, S2, S3, S4, and S5 basal surfaces separating the units.

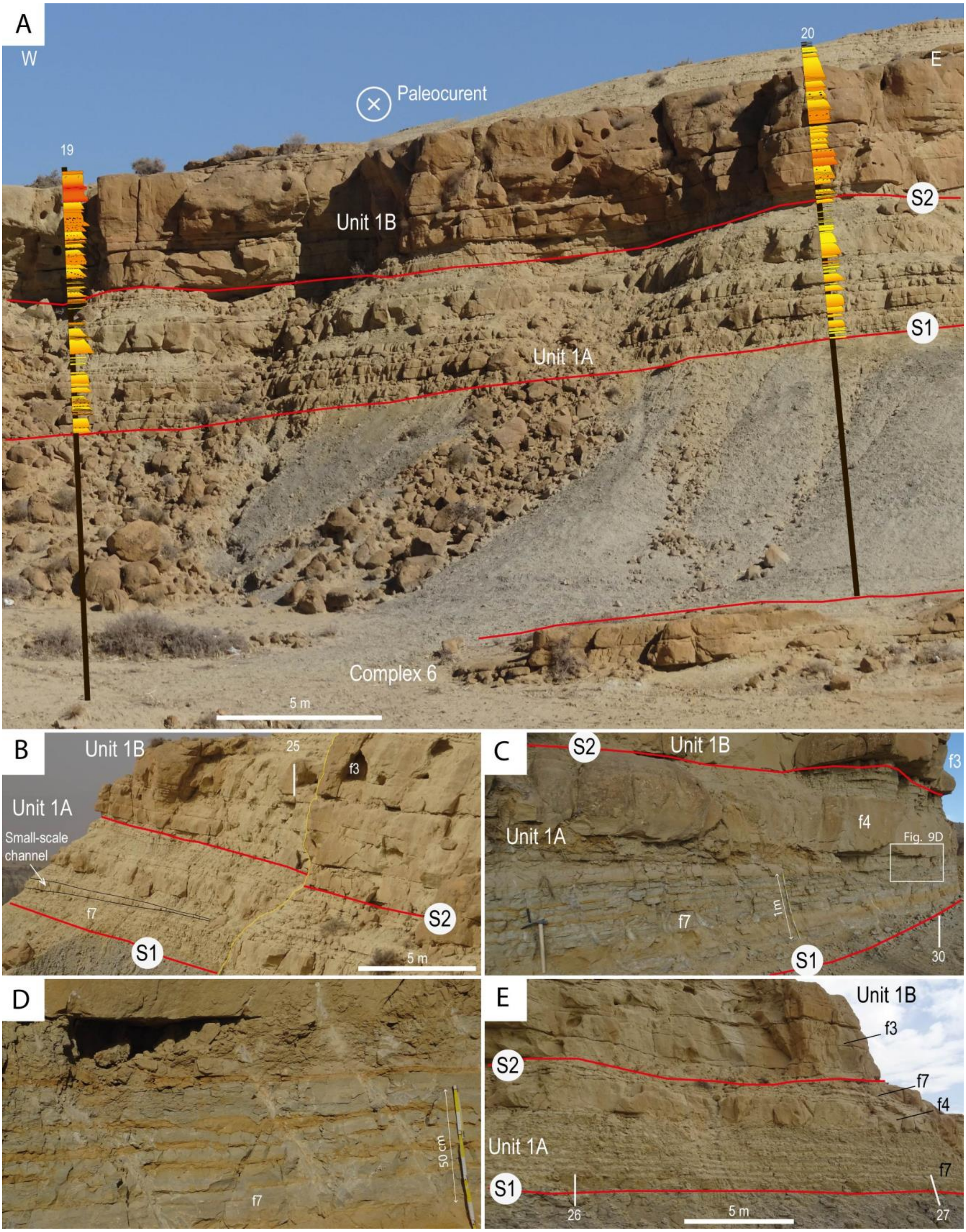

Fig. 9: A) View of units 1A and 1B (paleocurrent directed northward). B) Detail showing the channelized geometry of one of the sandy beds in Unit 1A interbedded with thin heterolithic beds (f7). C) View of Unit 1A composed of vertically stacked thin beds (f7) and thick

sandstones (f4). D) Detail of thin beds (belonging to facies f7) in Unit 1A. E) Differences between Unit 1A with thin heterolithic beds and thick sandstone bodies, and Unit 1B composed of thick sandstone bodies.

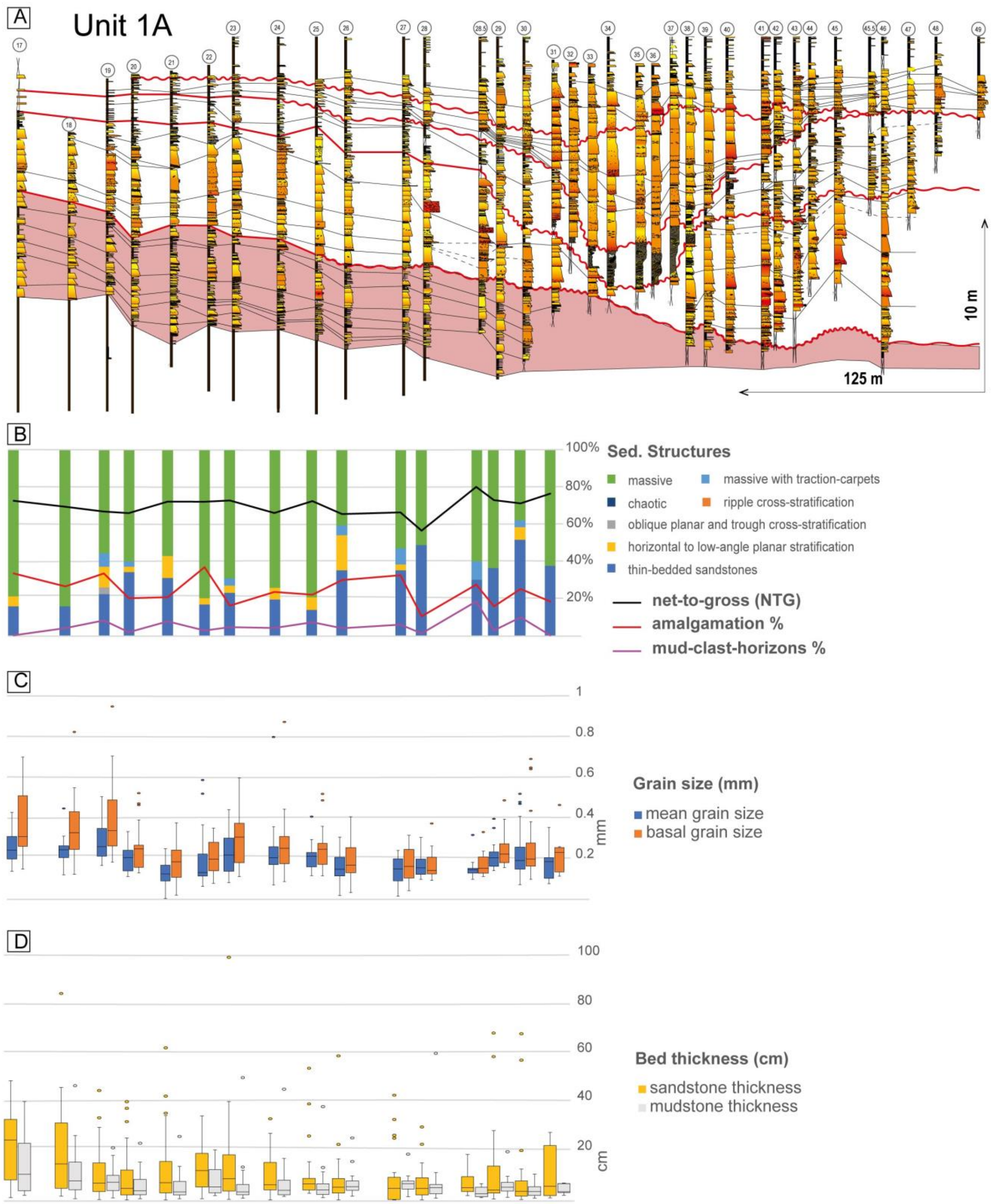

Fig. 10: A) Correlation panel with Unit 1A highlighted. B) Bar chart showing the percentage presence of sedimentary structures in Unit 1A, with the three line diagrams illustrating the percentage of NTG, amalgamation rate, and mud-clast horizons along the analyzed transect of Unit 1A. C) Box plots displaying the average grain size and basal grain size of the sandstone beds in Unit 1A. D) Box plots showing the thickness of sandstone and mudstone beds in Unit 1A. X axis of the plots refers to the measured logs shown just above in the correlation panel; Y axis refers to the entire unit; in the boxplots, dots refer to outlier values.

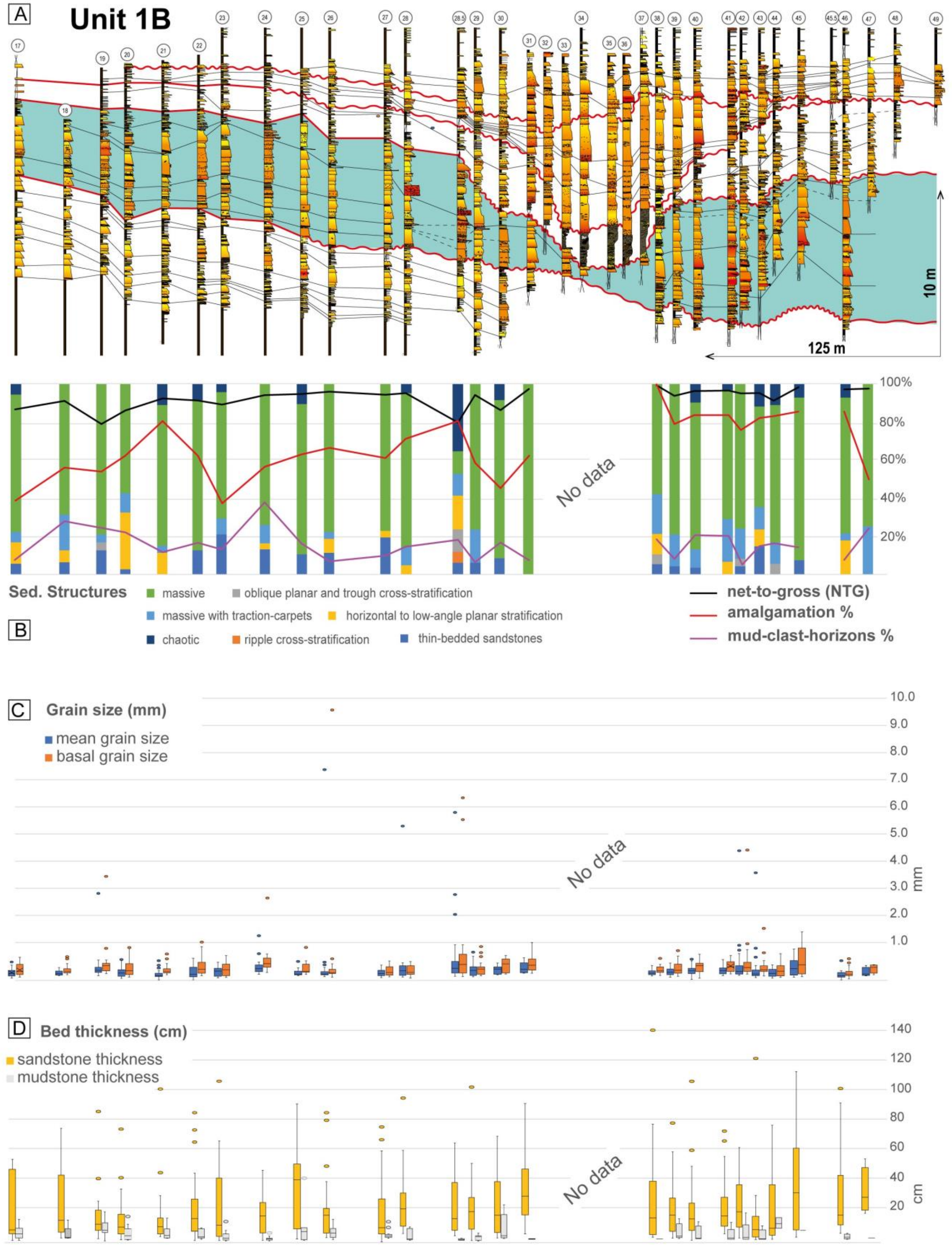
A
Unit 1B
10 m
125 m
100%
80%
60%
40%
20%
No data
Sed. Structures
massive
oblique planar and trough cross-stratification
massive with traction-carpets
horizontal to low-angle planar stratification
B
chaotic
ripple cross-stratification
thin-bedded sandstones
net-to-gross (NTG)
amalgamation %
mud-clast-horizons %
C
Grain size (mm)
mean grain size
basal grain size
mm
D
Bed thickness (cm)
sandstone thickness
mudstone thickness
cm

1258

Fig. 11: A) Correlation panel with Unit 1B highlighted. B) Bar chart showing the percentage presence of sedimentary structures in Unit 1B, with the three line diagrams illustrating the percentage of NTG, amalgamation rate, and mud-clast horizons along the analyzed transect of Unit 1B. C) Box plots displaying the average grain size and basal grain size of the sand beds in Unit 1B. D) Box plots showing the thickness of sand and mud beds in Unit 1B. X axis of the plots refers to the measured logs shown just above in the correlation panel; Y axis refers to the entire unit; in the boxplots, dots refer to outlier values.

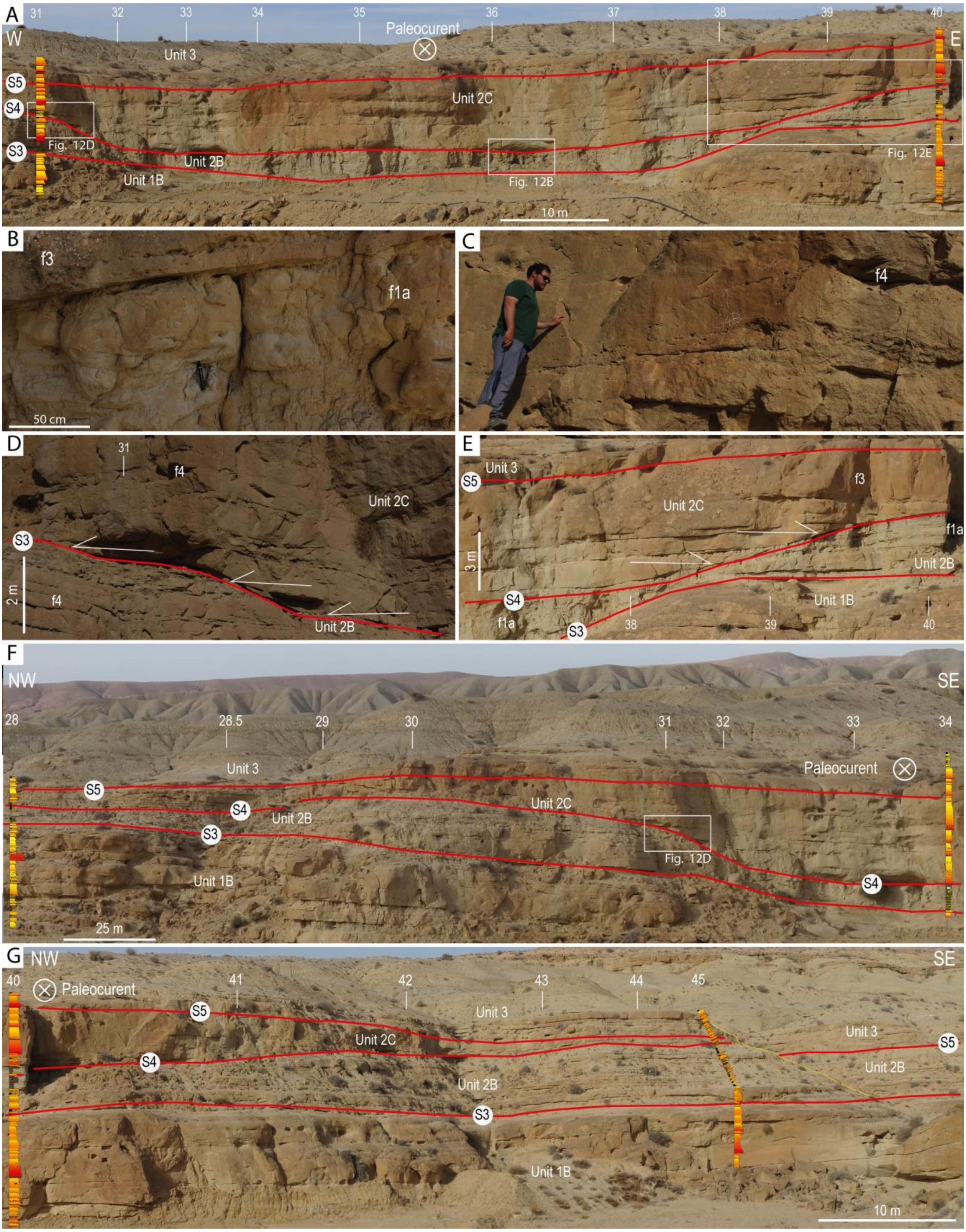

Fig. 12: A) Channel-fill displaying the zone with chaotic deposits of Unit 2B and the sandier thick-bedded zone of Unit 2C, along with part of Unit 3. B) Detail of chaotic deposits (f1a) and amalgamated sand beds (f3) in Unit 2B. C) Sandstone beds belonging to Unit 2B (f4).

D) Onlap relationships of Unit 2C against Unit 2B (S4 surface). E) Onlap relationships of Unit 2C against S4 surface. F) Western part of the channel of units 2B and 2C. Unit 3 at the top with thin bedded horizons. G) Eastern flank of the channel, showing the transition from thick sandstones (f3 and f4) of Unit 2C to thin beds (f6 and f7) and the erosion of Unit 3.

1274

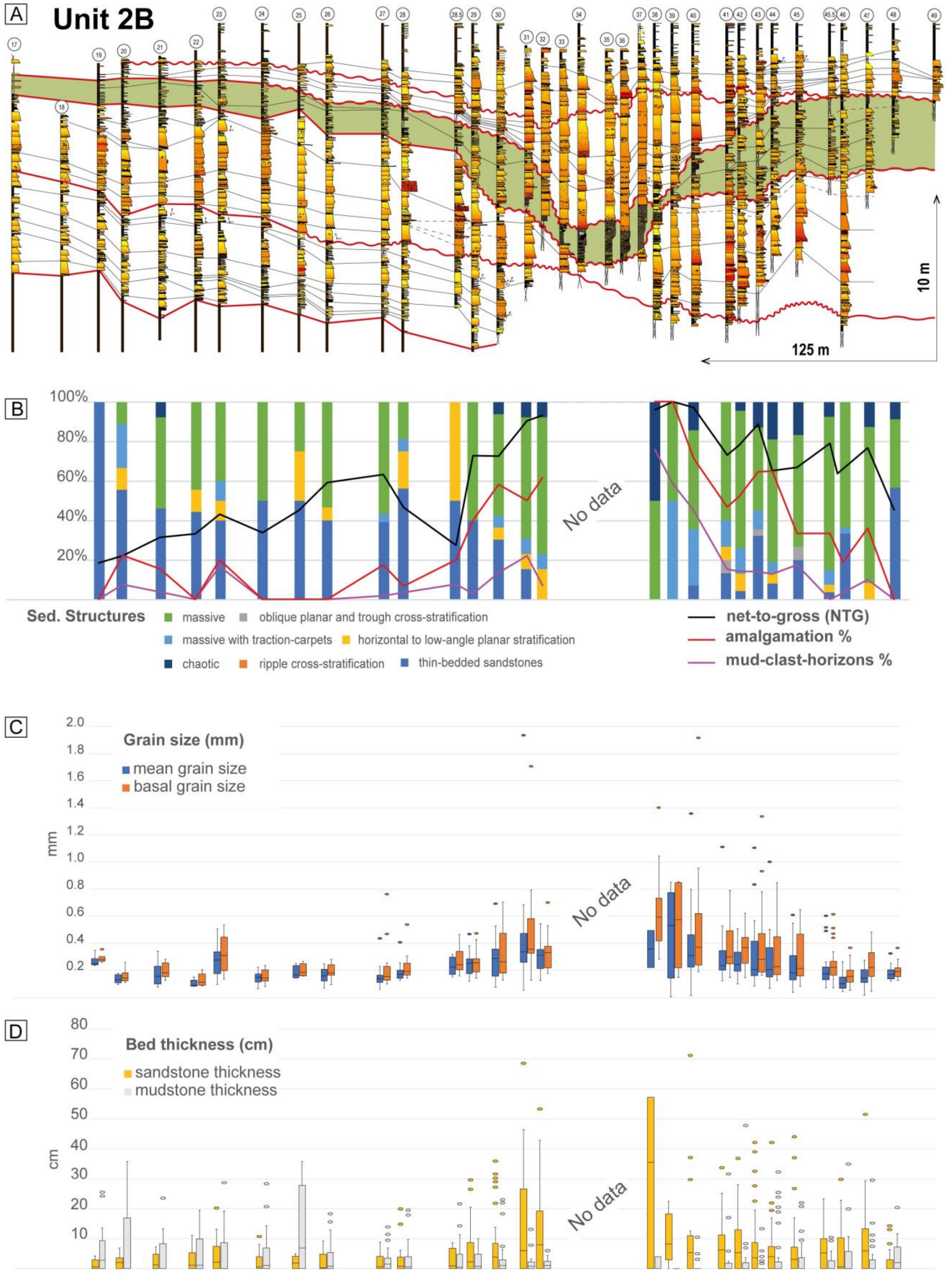
A
Unit 2B
10 m
125 m
B
No data
Sed. Structures
massive
oblique planar and trough cross-stratification
massive with traction-carpets
horizontal to low-angle planar stratification
chaotic
ripple cross-stratification
thin-bedded sandstones
net-to-gross (NTG)
amalgamation %
mud-clast-horizons %
C
Grain size (mm)
mean grain size
basal grain size
mm
No data
D
Bed thickness (cm)
sandstone thickness
mudstone thickness
cm
No data

Fig. 13: A) Correlation panel with Unit 2B highlighted. B) Bar chart showing the percentage presence of sedimentary structures in Unit 2B, with the three line diagrams illustrating the percentage of NTG, amalgamation rate, and mud-clast horizons along the analyzed transect of Unit 2B. C) Box plots displaying the average grain size and basal grain size of the sand beds in Unit 2B. D) Box plots showing the thickness of sand and mud beds in Unit 2B. X axis of the plots refers to the measured logs shown just above in the correlation panel; Y axis refers to the entire unit; in the boxplots, dots refer to outlier values.

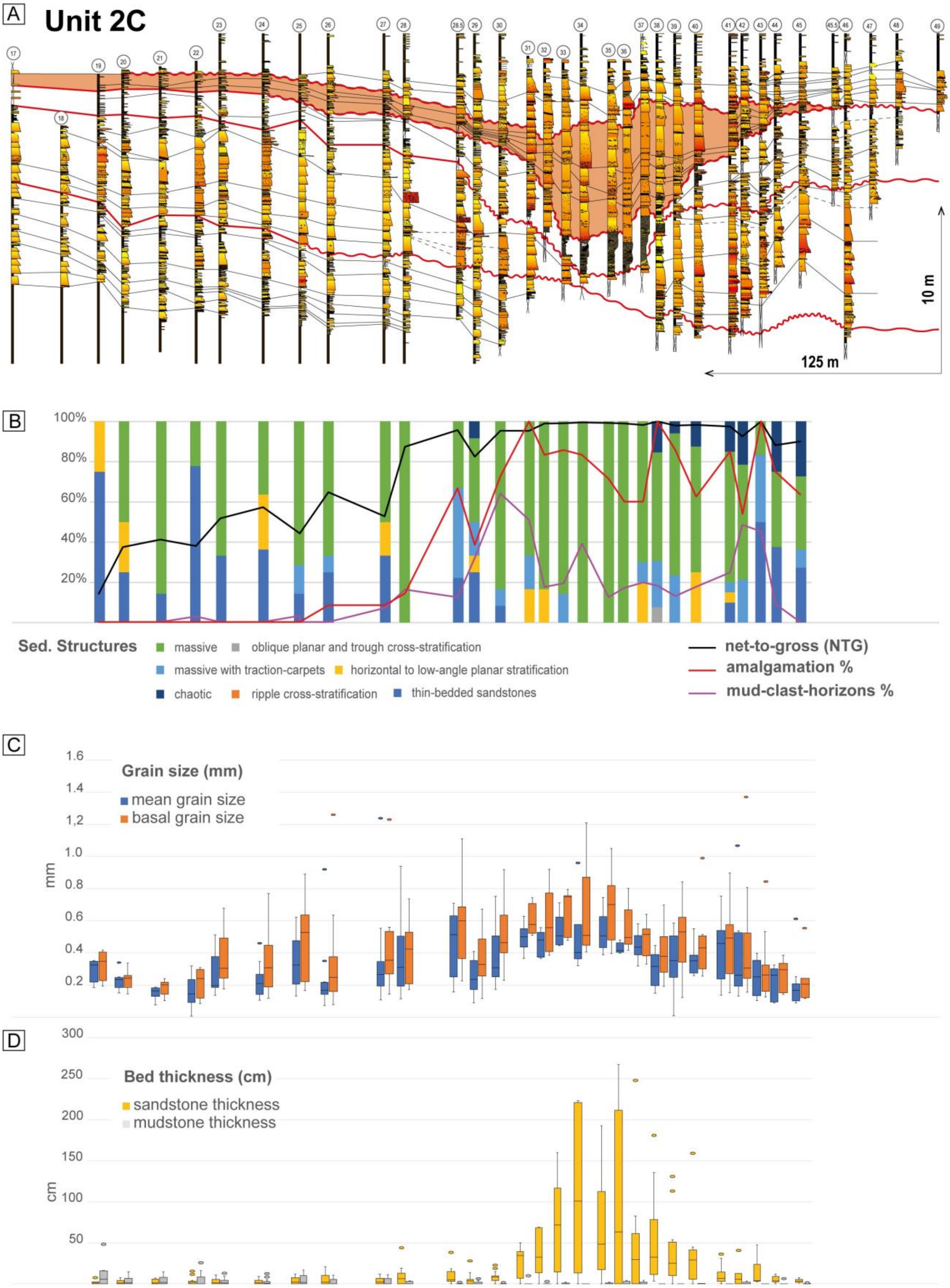

A
Unit 2C
10 m
125 m
B
100%
80%
60%
40%
20%
Sed. Structures
massive
oblique planar and trough cross-stratification
massive with traction-carpets
horizontal to low-angle planar stratification
chaotic
ripple cross-stratification
thin-bedded sandstones
net-to-gross (NTG)
amalgamation %
mud-clast-horizons %
C
Grain size (mm)
mean grain size
basal grain size
mm
1.6
1.4
1,2
1.0
0.8
0.6
0.4
0.2
D
Bed thickness (cm)
sandstone thickness
mudstone thickness
cm
300
250
200
150
100
50

1282

Fig. 14: A) Correlation panel with Unit 2C highlighted. B) Bar chart showing the percentage presence of sedimentary structures in Unit 2C, with the three line diagrams illustrating the percentage of NTG, amalgamation rate, and mud-clast horizons along the analyzed transect of Unit 2C. C) Box plots displaying the average grain size and basal grain size of the sand beds in Unit 2C. D) Box plots showing the thickness of sand and mud beds in Unit 2C. X axis of the plots refers to the measured logs shown just above in the correlation panel; Y axis refers to the entire unit; in the boxplots, dots refer to outliers values.

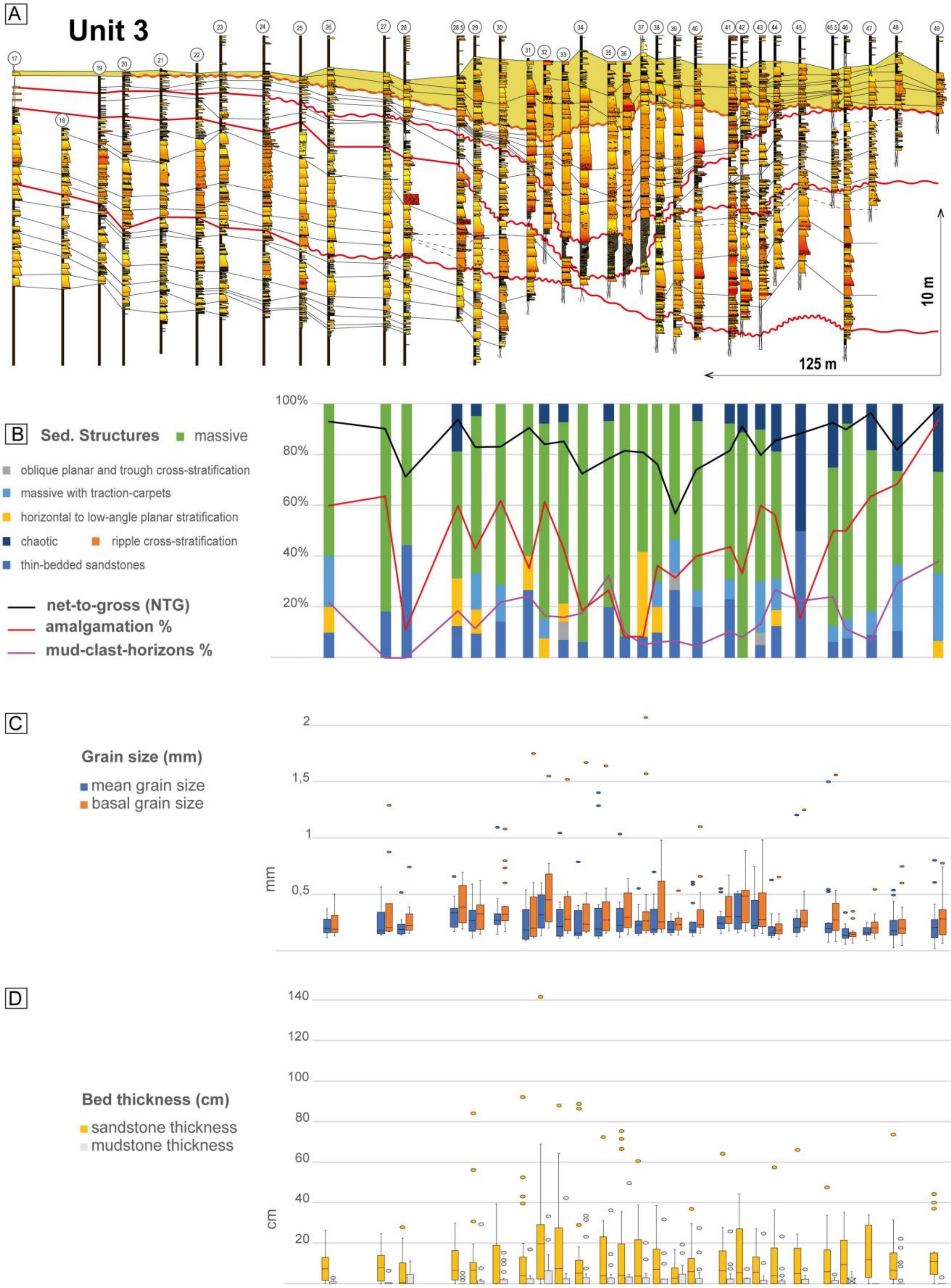
A
Unit 3
17
18
19
20
21
22
23
24
25
26
27
28
28.5
29
30
31
32
33
34
35
36
37
38
39
40
41
42
43
44
45
45.5
46
47
48
49
10 m
125 m
B
Sed. Structures
massive
oblique planar and trough cross-stratification
massive with traction-carpets
horizontal to low-angle planar stratification
chaotic
ripple cross-stratification
thin-bedded sandstones
net-to-gross (NTG)
amalgamation %
mud-clast-horizons %
100%
80%
60%
40%
20%
C
Grain size (mm)
mean grain size
basal grain size
2
1,5
1
0,5
mm
D
Bed thickness (cm)
sandstone thickness
mudstone thickness
140
120
100
80
60
40
20
cm

Fig. 15: A) Correlation panel with Unit 3 highlighted. B) Bar chart showing the percentage presence of sedimentary structures in Unit 3, with the three line diagrams illustrating the percentage of NTG, amalgamation rate, and mud-clasts horizons along the analyzed transect of Unit 3. C) Box plots displaying the average grain size and basal grain size of the sand beds in Unit 3. D) Box plots showing the thickness of sand and mud beds in Unit 3. X axis of the plots refers to the measured logs shown just above in the correlation panel; Y axis refers to the entire unit; in the boxplots, dots refer to outliers values.

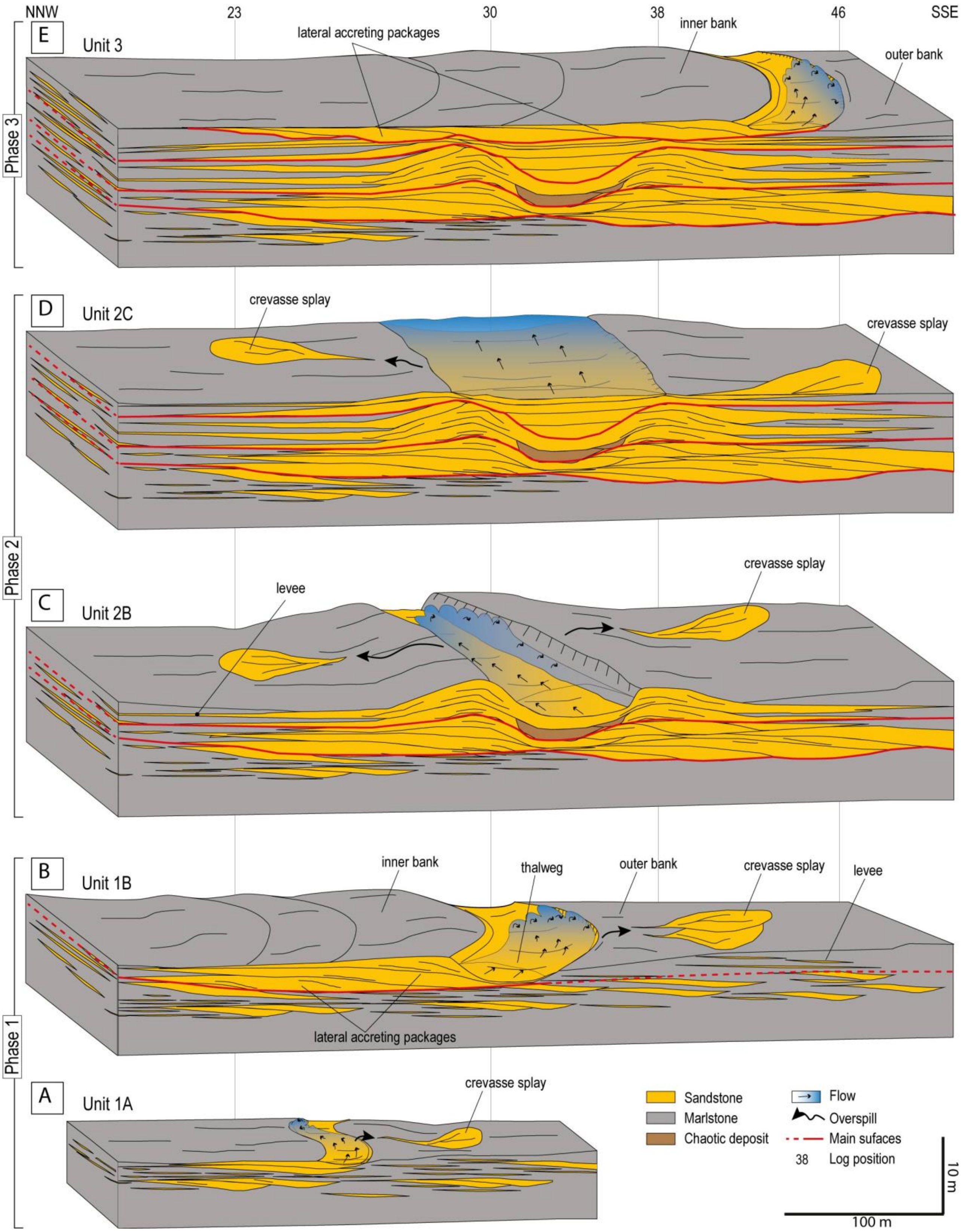

Fig. 16: Evolutionary model of the seafloor channels across the Complex 7 from Phase 1 to Phase 3. A) Initiation of the deposition; B) lateral expansion and channel migration; C) channel erosion; D) channel filling; E) lateral migration.

Table 1: Reservoir characteristics and distribution of the various architectural elements recognized in the studied part of Complex 7.

Architectural Element	NTG	Bed lateral continuity	Thickness	Sandstone connectivity	Facies	Facies Associations	Element area (%) vs. total complex area
Erosional channel-fill	> 0.9	Moderate (< 200 m)	1.5-9 m	Very good vertical and lateral connectivity due to paucity of fine-grained layers	f1a, f1b, f3, f4, and f5	FA1 and FA2	25
Laterally accreting	0.3-1.0	Moderate to fairly good (> 200 m)	1-3 m	Low connectivity in top-set part (FA 3) and good vertical and lateral connectivity in middle- and toe-set (FA 4 and FA 5)	f1c, f2, f3, f4, f5, and f6	FA3, FA4, and FA5	35
Overbank	0.2-0.3	Moderate to fairly good (> 200 m)	up to 5 m	Mud-rich intervals result in poor vertical and lateral connectivity	f6 and f7	FA6	40